# Shining Light on PAHs in Space

Andrews Mancilla, H.E.

# 2

# PAH Emission at the Bright Locations of PDRs: the GrandPAH hypothesis

The PAH emission observed in the Spitzer-IRS spectra of bright mid-IR locations of three well known reflection nebulae NGC 7023, NGC 2023 and NGC 1333 were analyzed. Each of these objects shows large variations in PAH band ratios when studied through spectral mapping. Nevertheless, the mid-IR spectra at these bright spots show a remarkably similar PAH emission spectrum. We used the NASA Ames PAH IR Spectroscopic Database to fit the observations and analyze the derived PAH populations. Our results show that PAH emission spectra in the 5–15 $\mu$m range appear to be rather insensitive to variations of the radiation field. Similar PAH populations of neutral small-to-medium sized PAHs ($\sim$ 50%), with ionized species contributing in slightly less than 50%, provide very good fits. Analyzing the degeneracy of the results shows that spectroscopic details place strong constraints on the PAH population. Subtle (but intrinsic) variations in the emission properties of individual PAHs lead to observable differences in the resulting spectra. On top of this, we found that variations of $<$ 30% in the PAH abundances would lead to noticeable spectral differences between the three PDRs. Therefore PAH populations must be remarkably similar at these different lines-of-sight. To account for this, we suggest the concept of grandPAHs as a unique mixture of the most stable PAHs emitting at these spots. This unique mixture would be a result of intense processing in the ISM. Using NGC 7023 as an example, the grandPAHs refer to the robust PAH population that results from the processing of PAHs at the border limit between the PDR and the molecular cloud where, due to the UV radiation that destroys the PAH population, the abundance of PAHs starts decreasing as we move towards the star.

H. Andrews, C. Boersma, M. W. Werner, J. Livingston, L. J. Allamandola & A. G. G. M. Tielens
*ApJ*, **Volume 807**, Issue 1, article id. 99, 24 pp. (2015)

## 2.1. Introduction

When observing the mid-IR spectra of gaseous and dusty regions in the sky, we can distinguish strong emission bands at 3.3, 6.2, 7.7, 11.3 and 12.7 $\mu$m, perched on emission plateaus at 7.0, 11.0 and 17.0 $\mu$m. In addition, many weak features can be observed at 8.6, 11.0, 12.0, 13.5, 14.0, 14.2, 15.9, 16.4, 17.4 and 17.8 $\mu$m. The carriers of these bands are nowadays accepted to be a class of organic molecules called polycyclic aromatic hydrocarbons (PAHs) (Léger & Puget 1984; Allamandola et al. 1985).

PAHs consist of hexagonal aromatic carbon rings with hydrogen atoms attached at the periphery. When exposed to high energy photons (up to 13.6 eV) PAHs get electronically excited; they increase their temperature considerably (reaching up to $\sim$1000 K); rapidly redistribute the absorbed energy among all available vibrational states; and relax, either by fragmenting or emitting IR photons through a fluorescence process.

Observational studies of PAHs have recently flourished with the available data from both Spitzer and Herschel space telescopes on UV illuminated environments such as photodissociation regions (PDRs). PDRs are the UV illuminated surfaces of molecular clouds, where the chemical reactions taking place are driven by the high energy UV photons that penetrate largely neutral atomic gas (Hollenbach & Tielens 1999). PDRs are bright in — among others— atomic fine structure lines of [O I] and [C II]; pure rotational lines of $H_2$ and (low-J) CO; UV pumped ro-vibrational transitions of $H_2$; PAH emission features, and mid/far-IR continuum emission associated with warm dust.

Much focus has been directed to the study of PDRs in reflection nebulae (RNe) as these are relatively benign, quiescent, extended regions (Young Owl et al. 2002), that allow us to observe more clearly the footprint of PAHs (e.g., Bregman & Temi 2005; Sellgren et al. 2007; Peeters et al. 2012). Spectral mapping of RNe, as well as spectral comparison of large samples of sources, provide a powerful tool to study the characteristics of interstellar PAHs. The variations observed between the C-C (6–9 $\mu$m region) and the C-H modes (10–15 $\mu$m) are generally attributed to variations in the degree of ionization of the emitting PAHs (e.g., Allamandola et al. 1999; Peeters et al. 2002; Galliano et al. 2008; and references therein). In contrast, variations among the C-H out-of-plane modes (11.3 and 12.7 $\mu$m bands) as well as variations between the 7.6, 7.8 and 8.6 $\mu$m bands are thought to result from variations in the molecular structure of the emitting PAH family (e.g., Hony et al. 2001; Peeters et al. 2012; Ricca et al. 2011; Ricca et al. 2012).

Laboratory studies and quantum chemical calculations have determined the IR spectra of a large number of PAH species. These have been compiled in The NASA Ames PAH IR Spectroscopic Database (PAHdb[1]; Bauschlicher et al. 2010; Boersma et al. 2014). The latest version (v2.00) contains 700 theoretically calculated and 75 experimental spectra of PAHs of different sizes ($N_c$ = 6–384 carbon atoms), ionization states, composition (including nitrogenated species) and structure (e.g., different hydrogen adjacency ratios). PAHdb also provides a suite of IDL scripts (AmesPAHdbIDLSuite) that allows users to handle the database in a practical and easy way (Boersma et al. 2014). Several works have used the AmesPAHdbIDLSuite to fit observational data (e.g., Cami 2011; Rosenberg et al. 2011; Boersma et al. 2013), and proved how insightful this approach is.

[1] http://www.astrochem.org/pahdb

Table 2.1: Brightest mid-IR Locations of the PDRs Studied in this Work.

| Object | RA (J2000.0) | DEC (J2000.0) | $F_{11.3\mu m}$ [a] | Observation Date | Position Angles |
|---|---|---|---|---|---|
| NGC 7023 NW | 21 01 32.5 | +68 10 25.7 | 2.21 | 2004-08-29 | 66.13 |
| NGC 2023 | 05 41 41.0 | −02 15 41.7 | 1.21 | 2004-10-04 | 178.43 |
| NGC 1333 | 03 29 20.7 | +31 24 33.0 | 0.32 | 2005-02-06 | -15.31 |

[a] Peak flux of the 11.3 $\mu$m feature after continuum subtraction, in Jy units.

In this work, we analyze the mid-IR spectra of the PDRs of three well-studied RNe: NGC 7023, NGC 2023 and NGC 1333. We carefully selected bright spots of PAH emission in the PDRs, that probe the transition of the molecular clouds to the cavities surrounding the stars. The spectra were obtained with the Spitzer Infrared Spectrograph (IRS; Houck et al. 2004). Long slit spectra were obtained along rims particularly bright in the mid-IR (Werner et al. 2004), and the spectra of the pixels of interest were extracted from the long slit data. Our focus is on the PAH emission, and so we use PAHdb to fit the astronomical spectra and analyze the derived PAH populations. We are particularly interested in these spectra, since they look strikingly similar in terms of PAH emission, considering that these are different objects and all present large variations of the PAH emission within themselves. Werner et al. (2009) originally pointed out the similarity of the slit spectra in these three nebulae. Here we study the similarity in the PAH emission from PAHdb standpoint, and we propose the *grandPAHs* as a plausible explanation to the results derived from PAHdb.

The concept of *grandPAHs* has been defined in Tielens (2013) as a set of the most stable PAH species that are able to survive the intense processing in the ISM, and as such, dominates the PAH population in space. This was proposed in order to explain the relatively constant 15–18 $\mu$m emission band patterns, and the overall homogeneity of PAH emission observed in different interstellar sources. Even though the *grandPAHs* have been mentioned in several works (e.g., Berné et al. 2009; Ali-Haïmoud 2014), up until now this hypothesis has not been explored in any way. This is the first attempt to do this. The simple geometry and well-determined physical conditions in the three RNe studied here, offer a great opportunity to examine the *grandPAH* hypothesis, using our current knowledge on PAH emission spectra through the use of PAHdb.

The outline of this work is the following: section 2.2 presents the data of the RNe studied in this work. In section 2.3 we present the motivation of this work. Section 2.4 discusses PAHdb and the assumptions we consider before performing the fits. The results are presented in section 2.5, while the implications of our results are discussed in section 2.6. In this last section we explore the concept of *grandPAHs* and propose a new interpretation about their role in the evolution of carbonaceous material in RNe.

## 2.2. Observations

### 2.2.1. Selected PDRs

**NGC 7023** This is a well-studied RN illuminated by the Herbig Be star HD200775. Our study focuses on the brightest mid-IR spot located in the North-West PDR (NW), 45" from the exciting star (see Table 2.1). NGC 7023 NW is often considered as the prototype of a PDR since it has an edge-on structure, which shows a clear stratification of the emitting region. The star has created a low density cavity which is surrounded by a dense molecular cloud. The cavity wall is lined by a thin H I layer (Fuente et al. 1998). The fullerene abundance increases rapidly into the cavity while the PAH abundance decreases from the PDR front towards the star (Sellgren et al. 2010; Pilleri et al. 2012; Berné & Tielens 2012). Table 2.2 lists the physical parameters taken from the literature determined for this location. Analysis of the observed far-IR continuum intensity yields an incident UV field of $G_0$ = 2600 Habing field units in the NW PDR (Chokshi et al. 1988). This is in agreement with the stellar flux at the projected distance (Alecian et al. 2008). Okada et al. (2013) reported a larger value of $G_0$ = 7700 from integrating the total IR emission from 3–1 100 $\mu$m. However this assumes spherical symmetry and it is presented as an upper limit. The gas density $n_H$ and temperature $T_{gas}$ listed in Table 2.2 have been estimated from the observed line intensities of [O I] 63 $\mu$m and [C II] 158 $\mu$m (Young Owl et al. 2002; Chokshi et al. 1988). The derived gas density in the PDR is in good agreement with the H I observations (Fuente et al. 1998).

**NGC 2023** This RN located in Orion, just below the Horsehead nebula, is illuminated by the B1.5V star HD37903, at a distance of 350 pc (Mookerjea et al. 2009; Sheffer et al. 2011). Our position is located 39" east of the star, and it is the brightest spot along one of the brightest rims observed at 8 $\mu$m (Peeters et al. 2012). The physical parameters considered for this position have been taken from the work of Steiman-Cameron et al. (1997). They determined $T_{gas}$, $n_H$ and $G_0$ for a position 42" south-east of the star (position P4 in their paper). This is the closest one to ours, and it falls along the clumpy rim where the peak of the mid-IR continuum (and cooling line emission) is observed. The value of $G_0$ = 15 000 for P4 was obtained from the FIR continuum. Using this value and considering a dilution that goes as the square of the projected distance to the star, we get $G_0$ = 17 400 for our position. The estimates of the gas density and temperature were derived using the cooling lines. However a comparison with PDR models shows there is a better agreement when assuming a clumpy structure of density $10^5$ cm$^{-3}$ and temperature of 750 K; and thus here we adopt these values instead (Table 2.2).

**NGC 1333** This is a highly active star forming region in the Perseus molecular cloud. Here we study the brightest mid-IR spot as observed at 8 $\mu$m, which is in the nebula illuminated by the late B star BD+30°549. This is not where the far IR peak is, which is in the nebula illuminated by SVS-3. The parameters listed in Table 2.2 have been taken from Young Owl et al. (2002). They derived physical conditions for the nebulae where our brightest spot is, based on far-IR observations with Kuiper Airborne Observatory (KAO). According to the far-IR dust continuum emission they derived $G_0$ = 4800. The gas density and temperatures were obtained from comparing the cooling lines ratio with the models of Tielens & Hollenbach (1985).

Table 2.2: Physical Conditions in Different PDRs Taken From the Literature

| Property | NGC 7023 NW | NGC 2023 | NGC 1333 |
|---|---|---|---|
| Central Star | HD 200775 | HD 37903 | BD+30°549 |
| Star Type | B2.5 Ve[a] | B1.5 V[e] | B9V[f] |
| Star Temperature (K) | 17000[a] | 23000[d] | 14000[f] |
| Distance from Star (") | 45 | 39 | 27 |
| $G_0$ | 2600[b] | 15000[d] | 4800[f] |
| Dust Temperature (K) | 50[c] | 50[d] | 45[f] |
| Gas Temperature (K) | 200[c] | 750[d] | 690[f] |
| Gas density ($cm^{-3}$) | $4\times10^{3}$[c] | $10^{5}$[d] | $2\times10^{4}$[f] |
| Ionization Parameter* $\gamma$ | $6.5\times10^{4}$ | $3.4\times10^{4}$ | $4.5\times10^{4}$ |

[a] Rogers et al. (1995); [b] Pilleri et al. (2012); [c] Chokshi et al. (1988); [d] Steiman-Cameron et al. (1997); [e] de Boer (1983); [f] Young Owl et al. (2002).
* The ionization parameter is defined as $\gamma \equiv G_0 \sqrt{T_{gas}}/n_e$, where the electron density has been calculated assuming that all free electrons come from singly ionized carbon, using the diffuse ISM gas-phase carbon abundance of $1.4\times10^{-4}$ (Cardelli et al. 1996).

### 2.2.2. Data Collection and Reduction

The spectra of the three nebulae were obtained as part of Spitzer GTO Program #19, PI M.Werner. The observation dates and positions observed are shown in Table 2.1 (note however, that the IRS spectra of NGC 7023 shown in Werner et al. (2004) were obtained under a separate Early Release Observation program; the NGC 7023 data shown here were obtained somewhat later in the mission and with a different slit position angle). Spectra were obtained for each nebula using both the 1st and 2nd order slits of the IRS short-low module (Houck et al. 2004). First order runs from 7.4 to 14 $\mu$m, and second order from 5.2 to 7.7 $\mu$m. Each IRS slit is 58" long in the spatial dimension and 3.6" wide in the dispersion direction. The extension of the spectra to 15 $\mu$m was scaled from a Spitzer long-low spectrum. For a given slit, spectra are obtained first with the telescope at a nominal position, and next with the telescope nodded half the slit length but along the slit, so that the two slit positions overlap. The RNe are bright enough that we chose to analyze data from only one of the slit positions. The on sky integration time for the spectra analyzed here is 44 sec.

The data reduction is carried out by downloading the calibrated two dimensional image frames and ancillary data from the Spitzer archive at IRSA. The reduction was done using Cornell University SMART data reduction program[2], which coadds the separate frames into a final image from which spectra at particular positions along the slit can be extracted. It is also possible to obtain a total spectrum summed along the slit. For this program, we extracted the spectrum of a region 4 pixels in length and two pixels wide (in the dispersion direction) centered at the position listed in Table 2.1 for each nebula. Thus the field of view is a rectangle 3.6"×7.2" in size. For each nebula, Table 2.1 gives the position angle of the

[2] http://isc.astro.cornell.edu/IRS/SmartRelease

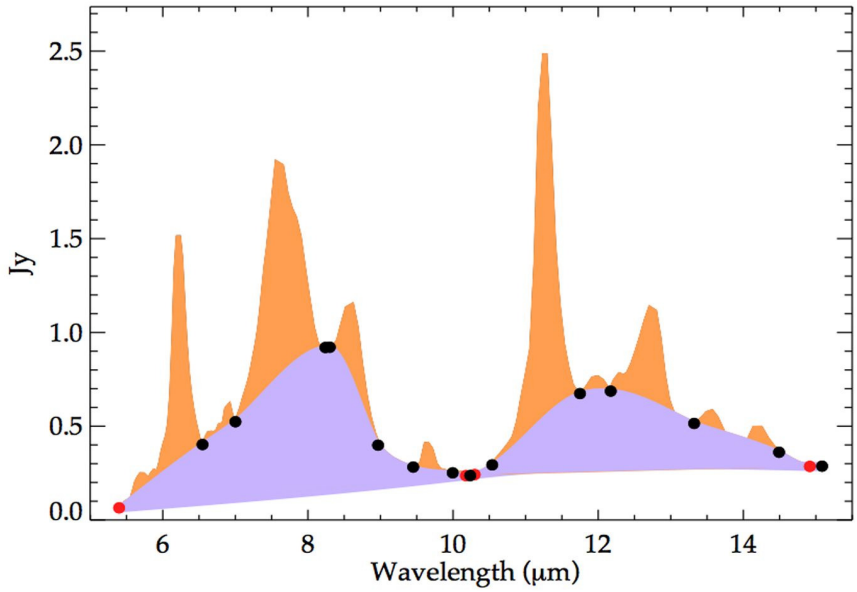


Figure 2.1: Schematic of Spline Decomposition Procedure. The spectrum corresponds to the brightest location in the NW PDR of NGC 7023. Red dots indicate the *anchor points* used to define the dust continuum. Black dots indicate *anchor points* used to define the emission from the first (6–10 $\mu$m) and second (10–15 $\mu$m) plateaus. The purple area then shows the plateau emission, while the orange area depicts the emission lines and PAH bands. See 2.2.3 for details.

slit, which is the orientation of the long side of the 3.6"×7.2" field of view. The spectra were extracted separately for the two orders and matched at the boundary (7 $\mu$m) where they overlap spectrally for a few tenths of a micron. Because of the brightness of the source and the fact that a baseline was extracted from the spectra before the analysis was begun, we did not do a sky subtraction. The uncertainties in the inferred flux are dominated by possible systematic rather than by statistical errors. To obtain an estimate, we have compared the independent measurements in the two nods of the spectrum of NGC 1333, which is the faintest of the sources. We find that the two spectra agree to well within 5% on average. On this basis, we estimate that the one-sigma uncertainty in our measurements is no more than 3% per data point.

### 2.2.3. Description of Removal of Continuum and Plateaus

There are different ways of decomposing and retrieving the PAH band strengths from the mid-IR spectra of astronomical objects. The methods depend basically on whether plateaus are considered as an inherent part of the narrow PAH bands (Sellgren et al. 2007; Smith et al. 2007) or as a separate component which may or may not be related to PAHs. As described in Boersma et al. (2012) and Peeters et al. (2012) the 10–15 and 15–18 $\mu$m plateaus vary independently from most of the narrower PAH bands. Therefore we consider plateaus and features separately, using spline functions to describe the plateaus, while PAH bands are described through Gaussian profiles. It is important to mention that extensive analysis on the variation of the PAH band ratios has shown that general trends are the same irrespective of the method used (Galliano et al. 2008).

Figure 2.1 presents a schematic of a spectrum analyzed using our decomposition method. The procedure was carried out as follows: first the continuum underneath the plateaus and PAH bands is removed by fitting a *continuum spline*, using as anchor points the local minima at 5.5, 10.3, 10.5 and 15.0 $\mu$m (see red dots in Figure 2.1). These are referred to as the *Features+Plateaus* spectra, since they contain both the PAH bands and the underlying plateaus.

A *plateau spline* was then fitted to the *Features+Plateaus* spectra to distinguish the plateaus (see purple area in Figure 2.1) from the individual PAH bands and emission lines (see orange area in Figure 2.1). Each *plateau spline* was defined by anchor points at around 5.5, 6.6, 7.2, 8.1, 8.4, 8.8, 9.4, 9.9 and 10.3 $\mu$m for the features rising above the *first plateau* between 6–10 $\mu$m; and at 10.3, 10.5, 11.8, 12.2, 13.2, 14.5 and 15.0 $\mu$m for the features of the *second plateau* at 10–15 $\mu$m (see black dots in Figure 2.1). This set of anchor points isolate the emission lines and PAH bands. These spectra are referred to as the *Features-Only* spectra.

In order to quantify the integrated intensities for later use, once the *plateau splines* were subtracted from the spectra, the narrow emission lines and PAH bands were fitted using multi-gaussian profiles. In order to do this, we used the least squares curve fitting routine MPFITFUN on IDL, which uses the Levenberg-Marquardt algorithm to minimize the $\chi^2$ (Markwardt 2009).

The narrow emission lines of $H_2$ S(6)–S(2) were then subtracted from both *Features +Plateaus* and *Features-Only* spectra, in order to isolate the emission coming from PAH features and plateaus. The spectra were finally rebinned on a wavenumber grid with a spacing of 5 $cm^{-1}$ following Boersma et al. (2013). Given the uncertainty in the band profile of PAHs and the unknown nature of plateau carriers (and their possible relation with PAHs), throughout this work all results will be presented for *Features+Plateaus* spectra. The fits to *Features-Only* spectra lead to very similar results and can be found in Appendix 2.A, together with a comparison to the *Features+Plateaus* spectra. Although most of the work in this paper is done with normalized spectra, we also give in Table 2.1 the flux (in Jy) at the peak of the 11.3 $\mu$m PAH feature above the baseline of the *Features+Plateaus* spectrum. This establishes a flux scale for each spectrum, which will permit future analysis to determine the abundance of the various PAH species along the observed line of sight.

## 2.3. Motivation

Figure 2.2 presents the *Features+Plateaus* spectra before removing the $H_2$ lines. The top panel shows the normalized spectra, while the bottom panel shows the difference between each normalized spectrum with the average of all three.

Inspection of Figure 2.2 reveals that the spectra are very similar to the smallest details; not just in terms of the presence of the same aromatic IR bands, but also the PAH band ratios. The differences with respect to the average are less than 10%, with the largest differences in the peak flux and band profile of the 6.2 and 7.7 $\mu$m features. We note that the spectra along the full slit —aligned with bright rims— are all very similar to those of the hot spots. This contrasts with the fact that large spectral variations have been observed across these nebulae (e.g., Berné et al. 2009; Rosenberg et al. 2011). *It is important to note that this similarity is not affected by whether plateaus are taken into account or not.*

This impressive spectroscopic similarity poses an important question. Why do the mid-IR spectra of these bright locations of the PDRs in these RNe resemble each other to such a high degree? All the more, when taking into account the different physical conditions and histories of the exciting stars (see Table 2.2). To gain insight into the PAH populations and physical conditions that might give rise to the same PAH spectrum, we use PAHdb to decompose the PAH emission into contributing PAH subclasses, namely: size, charge, composition and hydrogen adjacency (structure); and use an appropriate PAH emission model.

## 2.4. Method

The spectra shown in Figure 2.2 were analyzed using version 2.00 of PAHdb which comprises 700 theoretically computed PAH spectra. In order to perform the fit, we used the AmesPAHdbIDLSuite provided by PAHdb. The fitting routine in this case uses a non-negative least-square approach that solves $A\,x = b$ (where $A$ is the matrix of PAH spectra

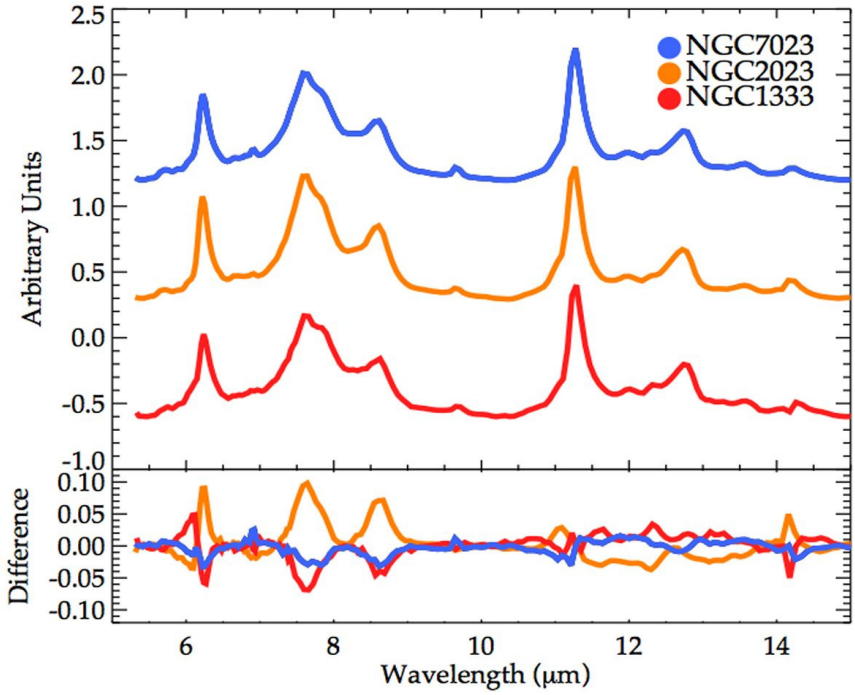


Figure 2.2: *Features+Plateaus* spectra of the brightest locations in NGC 7023, NGC 2023 and NGC 1333 before removing the $H_2$ lines. The *top panel* shows the normalized spectra plotted on an arbitrary scale for comparison. The *bottom panel* shows the difference between each normalized spectrum with the average of all three spectra using the same color scheme. As clear from this figure, all spectra look remarkably the same. In terms of PAH emission only, the largest differences between the individual spectra with the average are only a few percent, with the largest deviations associated with the profile of the 6.2 and 7.7 $\mu$m features ($<10\%$). The spectra also differ only slightly in the $H_2$ emission lines, as it can be observed from the lines $H_2$ S(5) 6.9 $\mu$m, S(3) 9.7 $\mu$m, and S(2) 12.3 $\mu$m.

and $b$ is the observed spectrum), by minimizing the Eucledian norm while forcing all coefficients $x$ to remain non-negative (Lawson & Hanson 1974). The suite also provides useful routines to model the emission of PAHs upon the absorption of a single photon. Here we have extended these routines to take more physical detail into account, admitting the entire spectrum of photons emitted by a star instead of considering a single photon energy.

### 2.4.1. Model Parameters

When using the PAH absorption spectra in PAHdb to fit astronomical spectra, we have to take the following into account: 1) the radiation field that excites the mixture of PAHs; 2) the stepwise nature of the emission process; 3) the profile and full-width-at-half-maximum (FWHM) of the emitted bands; and 4) the shift of the bands arising from anharmonic effects.

*Radiation Field*: PAHs emit in the mid-IR after absorption of UV-vis photons. For the regions studied here, we can assume single photon events (Tielens 2005). In the Ames-PAHdbIDLSuite, PAHs absorb a photon of an energy equal to the average photon energy emitted by the star. This is computed from considering the stellar spectrum together with the PAH absorption cross sections (from Li & Draine 2001). However, a more complete approach —though more time consuming— is to consider the entire spectrum of photons emitted by the star. Here we use this approach using Kurucz stellar atmosphere models to describe the emission of each star according to the parameters given in Table 2.2. We assume a solar metallicity model, and a surface gravity of $\log(g)$ =4 for all three stars (Kurucz 1993). We consider each PAH absorbs photons of energies up to $E_{max}$ = 13.6 eV.

*Emission Model*: Prior to absorbing an exciting photon, each PAH is assumed to be in its ground electronic (and vibrational) state at a temperature considered to be that of the cosmic microwave background $T_{ini}$ = 2.73 K. We note however, that the emission spectrum does not depend strongly on the assumed initial temperature. In the environments studied here collisional excitation and multiphoton events are unimportant compared to single UV photon excitations.

After photon absorption, a PAH attains a maximum temperature $T_{max}(E)$ that depends on the energy absorbed, and the heat capacity of the PAH in question, $C_v(T)$. This heat capacity and the consequent cooling rate $dT/dt$ are here calculated using the so-called thermal approximation (e.g., Schutte et al. 1993; Bakes et al. 2001) just as considered in PAHdb. In this approximation, the emission from a given vibrational mode is calculated as the average emission of an oscillator connected to a thermal bath at $T$. Thus the Boltzmann equation is used to describe the excitation process, and both $C_v(T)$ and $dT/dt$ are calculated using the frequencies, $\bar{\nu}_i$, of all the vibrational modes of each PAH. The maximum temperature attained is then calculated from:

$$\int_{T_{ini}}^{T_{max}(E)} C_v(T)dT = E \tag{2.1}$$

In order to model the relaxation process we consider the temperature probability distribution function $G(T)$ from Bakes et al. (2001), which considers the emission process as a Poisson process, leading to an exponential distribution of the cooling times (see also Aannestad & Kenyon 1979; Purcell 1976) given by:

$$G(T,E) = \frac{\bar{r}}{dT/dt} \exp(-\bar{r}\tau_{min}(T,E)) \tag{2.2}$$

Where $\bar{r}$ corresponds to the average photon absorption rate, and $\tau_{min}$ corresponds to the minimum amount of time the PAH spends at a temperature $T$ after reaching $T_{max}(E)$. Since we consider that PAHs can absorb photons of different energies $E = h\nu$, the $G(T)$ function has to be integrated over the photon spectrum under consideration. This depends on both the stellar spectrum $F_\nu$ and the absorption cross section of each PAH $\sigma_{abs}(\nu)$, which here is taken from Li & Draine (2001). The relaxation process then lasts until each PAH returns to its initial temperature $T_{ini}$. The emission from a given mode $I_i$ then can be described as:

$$I_i = 4\pi \int \sigma_{\bar{\nu}_i} B(\bar{\nu}_i, T) \tilde{G}(T) dT \tag{2.3}$$

Where $\tilde{G}(T)$ is $G(T, E)$ averaged over the photon energies:

$$\tilde{G}(T) = \frac{1}{\bar{r}} \int G(T, E) n(E) dE \tag{2.4}$$

Here $\sigma_{\bar{\nu}_i}$ corresponds to the integrated infrared cross section of mode $i$, and $n(E)$ corresponds to the number of photons of energy $E$ absorbed by the PAH.

*Band Profile and FWHM*: The PAH band profile reflects intra/intermode anharmonicities coupled with the non-radiative vibrational redistribution process (e.g., Pech et al. 2002). As these processes are not well-understood, the profile to be adopted is uncertain. Typically either Lorentzian or Gaussian profiles are assumed. As the vibrational modes in a PAH are strongly coupled, Lorentzian oscillators do not provide a good description for the intrinsic profiles of these bands (Barker et al. 1987; Pech et al. 2002). Depending on the anharmonicity of the modes involved, the profiles may develop a strong red-shaded wing. If the emission bands arise from a broad mixture of related species, we can consider that the PAH species contributing to each band emit as oscillators randomly distributed around a mean, which leads to Gaussian band profiles. In terms of the width of the bands, we consider the same FWHM for all bands to be 15 $cm^{-1}$. This choice is based on experiments on small PAHs that have shown that, for short wavelength bands ($\lambda < 15\mu$m), typical widths range between 10–30 $cm^{-1}$ depending on the band in question. The instrumental FWHM of IRS low resolution spectra expected at these wavelengths is roughly 5 to 20 $cm^{-1}$, sufficiently similar for this work. See the Appendix for a further discussion on the band profile assumed in this study.

*Band Shifts*: Anharmonic effects induce a small redshift of the band positions. Experiments have only been performed on small PAHs (e.g., Joblin et al. 1995), and since what happens for larger PAHs is unknown, we consider a uniform shift for all bands of 15 $cm^{-1}$ as a first approximation (Cook & Saykally 1998; Pech et al. 2002; Boersma et al. 2013).

### 2.4.2. Database

Once the description of the emission process had been defined, decisions were made regarding the pool of PAHs to be considered in the fits. On this matter it is important to keep the characteristics of PAHdb in mind. These have been extensively discussed in Boersma et al. (2013). Here we summarize the relevant points as follows:

i) The database contains a large number of small PAHs with $N_c < 20$. Such small PAHs are assumed to be destroyed in the radiation fields considered here. Consequently, all species with less than 20 carbon atoms are removed from the initial pool of PAHs prior to the fit of the astronomical spectra.

ii) Regarding charge, one expects neutral and positively ionized PAHs to dominate the PAH population in PDRs where the ionization parameter $\gamma \equiv G_0 \sqrt{T_{gas}}/n_e > 10^4$. Most of the PAHs in the database are cations and neutrals, with only 12% of the entire database being singly ionized anions. While this would seem to be consistent with the expected population in the emission zone, fits can still result in high anionic abundances. This is because PAH anion bands are redshifted compared to the bands of their neutral/cationic counterparts. In effect, the fitting procedure uses anions to account for anharmonic redshifts of the bands.

iii) Concerning heteroatomic species, we only include PAHs that contain nitrogen atoms (PANHs). N-substitution has been suggested as one way of shifting the emission in the 6–6.5 $\mu$m region to the observed position of the 6.2 $\mu$m band (Hudgins et al. 2005). Given that there are still doubts about their formation process, in a way, PANHs may be viewed as representatives of any class of PAHs in which the C-C modes are shifted to 6.2 $\mu$m, e.g., pyramidal carbon or aliphatic structures (Galué 2014; Pino et al. 2008). Other heteroatomic PAHs are expected to be less stable, and thus we do not include them in the fits.

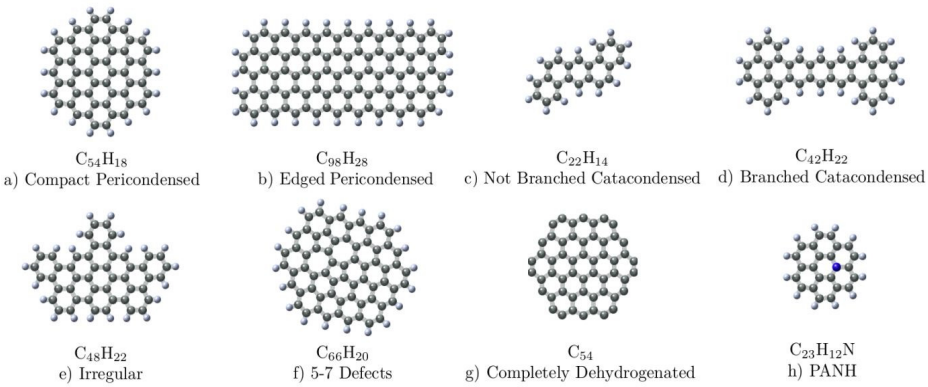


Figure 2.3: Structure classification of PAHs as typefied by one characteristic PAH (see text for details). a) Compact Pericondensed PAHs: These are PAHs with a compact core of carbon atoms with 12 duo-hydrogens and solo-hydrogens at the periphery. b) Pericondensed PAHs With Edges: These are pericondensed PAHs with edges containing trios. c) Not Branched Catacondensed PAHs: these are linear PAHs showing either only 8 quartets and solos (extremely linear) or admitting also duos (i.e., corners). d) Branched Catacondensed PAHs: these are linear PAHs containing trios (having branches). e) Irregular PAHs: these are PAHs whose shape do not follow any of the other classifications. They are mostly pericondensed PAHs with sharp edges (admitting trios and/or quartets). f) PAHs having the 5–7 fused ring defects. These are compact pericondensed PAHs. Their abundance contribution is already considered in the output values of the contribution of pericondensed PAHs listed in Table 2.4. g) Completely Dehydrogenated PAHs: These are PAHs with all hydrogens removed. h) Nitrogenated PAHs (PANHs): the nitrogen atom is always replacing one carbon atom from the core of the PAH.

iv) Lastly, PAHdb is dominated by pericondensed and symmetric PAHs. Stability studies have long shown that pericondensed and symmetric PAHs are in general more stable (in terms of chemical reactivity and fragmentation) than catacondensed PAHs (e.g., Stein 1978; Crawford et al. 1985; Ricca et al. 2011). This is due to the difference in the electronic density distribution and resonance energies of PAHs having different structures. Figure 2.3 shows the structure classification considered in this work. We have distinguished two types of *pericondensed* PAHs: *compact* (only solos and 12 duo-hydrogens at the periphery) and with *edges* (admitting trio-hydrogens). Likewise, we also distinguish between two types of *catacondensed* (linear) PAHs: *branched* (admitting trios) and *not branched* (8 quartets and solos and/or duos). Those that do not fall in any of these categories are considered as having *irregular* structure. We also recognize that PAHdb lacks enough large pericondensed PAHs with edge structure (i.e., trio and quartet-hydrogens). Since these are the PAHs necessary to properly describe the 15–20 $\mu$m region (Boersma et al. 2010; Ricca et al. 2010), we restrict our fits to the 5–15 $\mu$m range only. While we do not include the 15–18 $\mu$m region in our fitting procedure, we will come back to this spectral range in the discussion.

In view of the above, we have restricted the entire pool of (initially 700) PAHs available in PAHdb to include medium-to-large PAHs (i.e. $N_c > 20$); pure (carbon-and-hydrogen) PAHs and PANHs; and PAHs having no $CH_2$/$CH_X$ side groups (since these species are also expected to be underrepresented in PAHdb). This results in an initial pool containing 292 PAHs. The results derived from using this condition are presented in the next section and are referred to as the *base run* results. It is important to mention that all these PAHs are expected to have ionization potentials IP < 13.6 eV, following the IP $\propto (Z + 0.5) \times N_c^{-1/2}$ dependence described in Tielens (2005), where $Z$ is the ionization state of the PAH.

## 2.5. Results

The results are presented for *Features+Plateaus* spectra and only refer to NGC 7023, since —as the spectra are similar to a very high degree— the fits for all three spectra lead to the same results. The results for the other two RNe and the *Features-Only* spectra can be found in the Appendix 2.A.

First the *base run* results are presented. This is then followed by an exploration of the degeneracy in the fit, which provides insight into the allowed variation in both, the actual contributing PAH species and PAH subclasses.

### 2.5.1. Base Run

The fit to the NGC 7023 *Features+Plateaus* spectrum is shown in Figure 2.4. Table 2.3 lists all PAHs that make up the fit, together with their relative abundances, a brief description of their structure class, and whether the PAH is a radical or not. This set of PAHs comprises the *base run* fit to NGC 7023. Their structures are shown in the Appendix. Table 2.4 summarizes the breakdown of the fits to all PDR spectra in terms of size, ionization states, composition, and structure. The average photon energy has been derived convolving the stellar emission, with the absorption cross section of the PAHs. We have admitted in our fits dehydrogenated PAHs, and PAHs with Stone-Wales (five and seven fused rings) defects, referred to here as PAHs with *SW defects* (Stone & Wales 1986; Ricca et al. 2011). Their contribution is included in that of pericondensed PAHs.

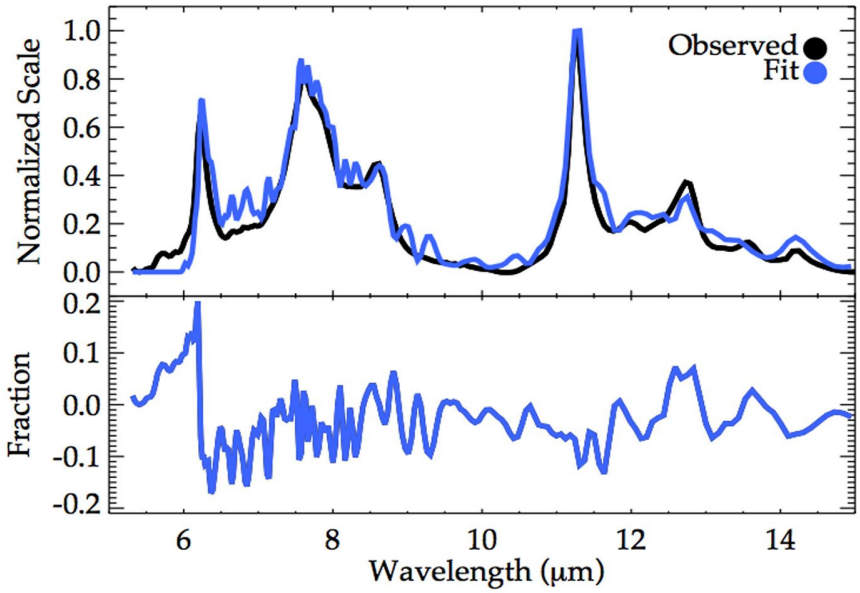


Figure 2.4: *Base run* fit to the *Features+Plateaus* spectrum of the brightest location in NW PDR of NGC 7023. The spectra are shown in normalized scale. The figure also shows the difference between both normalized spectra. Out of a pool of 292 PAHs, this fit requires only 33. Table 2.3 lists the PAHs used in this fit. The results of the *base run* for NGC 2023 and NGC 1333 can be found in the Appendix.

As observed from Figure 2.4 there are regions that are not well-reproduced by the fit. However these *problematic regions* do contain valuable information. The region at $\lambda < 6\,\mu$m is dominated by the emission from combination bands and overtones that are not included in the database (Boersma et al. 2009). The residual at $6.2\,\mu$m is usually attributed to the incompleteness of the database, related possibly to PANHs, pyramidal carbon or aliphatic groups (Hudgins et al. 2005; Galué 2014; Pino et al. 2008). The spectra available in PAHdb also do not fit well the weakest features, such as the $13.5\,\mu$m. This is because the database lacks the necessary variation in edge structure to reproduce the weak bands properly, while simultaneously satisfying all constraints posed by the dominant features between 5–$15\,\mu$m.

Perusal of Table 2.4 shows that the best fits to all three RNe spectra produce very similar results. In fact, the PAH population derived for all three PDRs is practically the same down to the derived abundances of the contributing species. Around 88% of the PAHs used to fit NGC 2023 are also used to fit the spectrum of NGC 7023, and they make up 98% of the total abundance of PAHs in the fit to NGC 2023. Similarly, the fit to NGC 1333 shares 88% of its PAHs with NGC 7023, contributing 94% to the total abundance of PAHs in the fit. Thus, all three fits essentially rely on the same set of PAHs.

The fact that we get very similar results highlights the similarity of the astronomical spectra, and the insensitivity of PAH emission spectra relative to the exciting radiation field. The three RNe studied here have different illuminating stars with effective temperatures ranging from $T_{eff}$ = 14 000 to 23 000 K. As a test run, we studied the effect of the radiation field on the emission spectrum of the *base run* PAHs, using Kurucz stellar atmosphere

Table 2.3: Base-run PAHs Derived From Fit to NGC 7023 Features+Plateaus Spectrum. See 2.5.1 for details.

| Uid[a] | Formula | Abundance (%) | $n_{solo}$ | $n_{duo}$ | $n_{trio}$ | $n_{quartet}$ | Structure[b] | R/NR[c] |
|---|---|---|---|---|---|---|---|---|
| 128 | $C_{36}H_{16}$ | 16.0 | 2 | 8 | 6 | 0 | Irregular | NR |
| 605 | $C_{66}H_{20}^{-}$ | 14.4 | 8 | 12 | 0 | 0 | 5–7 Ring defects | R |
| 620 | $C_{42}H_{16}$ | 9.3 | 4 | 12 | 0 | 0 | Pericondensed | NR |
| 226 | $C_{23}H_{12}N$ | 6.6 | 0 | 12 | 0 | 0 | Pericondensed | R |
| 600 | $C_{66}H_{20}$ | 5.5 | 7 | 10 | 3 | 0 | 5–7 Ring defects, with edges | NR |
| 157 | $C_{42}H_{22}^{-}$ | 4.8 | 6 | 4 | 12 | 0 | Catacondensed, branched | R |
| 11 | $C_{32}H_{14}^{-}$ | 4.5 | 2 | 12 | 0 | 0 | Pericondensed | R |
| 636 | $C_{48}H_{18}^{+}$ | 4.3 | 6 | 12 | 0 | 0 | Pericondensed | R |
| 255 | $C_{52}H_{18}N_2^{+2}$ | 3.3 | 6 | 12 | 0 | 0 | Pericondensed | NR |
| 243 | $C_{31}H_{14}N^{+}$ | 3.2 | 2 | 12 | 0 | 0 | Pericondensed | NR |
| 592 | $C_{32}H_{14}^{+}$ | 3.0 | 2 | 12 | 0 | 0 | 5–7 Ring defects | R |
| 284 | $C_{22}H_{12}$ | 2.6 | 0 | 6 | 6 | 0 | Irregular | NR |
| 704 | $C_{54}$ | 2.4 | 0 | 0 | 0 | 0 | 100% Dehydrogenated, pericondensed | R |
| 229 | $C_{23}H_{12}N$ | 2.2 | 0 | 12 | 0 | 0 | Pericondensed | R |
| 31 | $C_{24}H_{12}^{+2}$ | 1.9 | 0 | 12 | 0 | 0 | Pericondensed | R |
| 308 | $C_{22}H_{14}^{+}$ | 1.7 | 6 | 0 | 0 | 8 | Catacondensed, not branched | R |
| 639 | $C_{90}H_{24}^{+}$ | 1.7 | 12 | 12 | 0 | 0 | Pericondensed | R |
| 301 | $C_{22}H_{14}$ | 1.7 | 2 | 4 | 0 | 8 | Catacondensed, not branched | NR |
| 307 | $C_{22}H_{14}$ | 1.7 | 6 | 0 | 0 | 8 | Catacondensed, not branched | NR |
| 158 | $C_{42}H_{22}^{+}$ | 1.6 | 6 | 4 | 12 | 0 | Catacondensed, branched | R |
| 544 | $C_{32}H_{18}^{+}$ | 1.3 | 4 | 0 | 6 | 8 | Catacondensed, branched | R |
| 601 | $C_{66}H_{20}^{+}$ | 1.0 | 7 | 10 | 3 | 0 | 5–7 Ring defects, with edges | R |
| 632 | $C_{128}H_{28}^{-}$ | 0.9 | 16 | 12 | 0 | 0 | Pericondensed | R |
| 167 | $C_{112}H_{26}^{-}$ | 0.8 | 14 | 12 | 0 | 0 | Pericondensed | R |
| 181 | $C_{102}H_{26}^{+}$ | 0.7 | 12 | 8 | 6 | 0 | Pericondensed, with edges | R |
| 591 | $C_{32}H_{14}$ | 0.6 | 2 | 12 | 0 | 0 | 5–7 Ring defects | NR |
| 543 | $C_{36}H_{20}^{-}$ | 0.6 | 6 | 0 | 6 | 8 | Catacondensed, branched | R |
| 624 | $C_{170}H_{32}^{-}$ | 0.5 | 20 | 12 | 0 | 0 | Pericondensed | R |
| 707 | $C_{66}^{+}$ | 0.5 | 0 | 0 | 0 | 0 | 100% Dehydrogenated, pericondensed | R |
| 626 | $C_{40}H_{16}^{+}$ | 0.4 | 4 | 12 | 0 | 0 | Pericondensed | R |
| 257 | $C_{52}H_{18}N_2^{+2}$ | 0.4 | 6 | 12 | 0 | 0 | Pericondensed | NR |
| 614 | $C_{150}H_{30}^{-}$ | <0.1 | 18 | 12 | 0 | 0 | Pericondensed | R |
| 228 | $C_{23}H_{12}N^{+}$ | <0.1 | 0 | 12 | 0 | 0 | Pericondensed | NR |

[a] Unique identifier for each PAH in PAHdb. [b] The structures of these PAHs can be found in the Appendix. [c] R stands for radical species, NR stands for non-radical species.

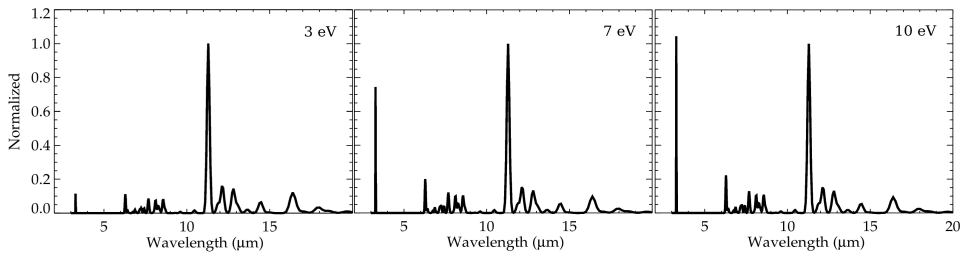


Figure 2.5: Computed emission spectrum of circumpyrene (the most abundant PAH in all *base run* fits) after absorbing a 3, 7 and 10 eV photon. These values correspond to the average photon energies absorbed by PAHs in fields illuminated by stars at $T_{eff}$ = 4 000, 17 000 and 35 000 K respectively. The emission spectra are shown normalized to the 11.3 $\mu$m band to illustrate how the relative band intensities vary with increasing (absorbed) photon energy.

models of main sequence stars with effective temperatures varying from 4 000 to 35 000 K. We then coadded their spectra using the original relative abundances listed in Table 2.3. The resulting spectra show little if any band intensity variations. The reason for this is illustrated with the spectra given in Figure 2.5. The computed emission spectrum of circumpyrene (one of the most abundant PAH in all *base run* fits) after absorbing a 3, 7 and 10 eV photon is shown in the left, middle and right panels respectively. These energies correspond to the average photon energies absorbed by PAHs in fields illuminated by stars at $T_{eff}$ = 4 000, 17 000 and 35 000 K respectively. We see that, using our emission model, the relative intensity of the 3.3 $\mu$m band to the other bands is the only ratio that is very sensitive to the effective temperature of the illuminating star. Unfortunately this band is not probed with IRS data, and in PAHdb its intensity can be 50% off (Langhoff 1996). We would like to emphasize then the importance of measuring the 3.3 $\mu$m band with the same aperture along the same line-of-sight as the longer wavelength spectrum, in order to get further information on the PAH population (see also Li & Draine 2001).

Concerning the relative abundance distribution of PAHs, the fitting procedure relies on a wide range of PAHs. The *base run* contains no single PAH with an abundance greater than 16%. The PAHs that contribute the most are the irregular-shaped closed shell 3,4;5,6;7,8;12,13-tetrabenzoperopyrene $C_{36}H_{16}$ (uid = 128), the *SW defect* radical of circumovalene $C_{66}H_{20}^{-}$ (uid = 605), and the non radical circumpyrene $C_{42}H_{16}$ (uid = 620), which —as a side note— is the most abundant PAH in the fits to *Features-Only* spectra (see Appendix 2.A). The abundances of these PAHs are between 9–16%. In fact, most of the PAHs contribute in small abundances < 5%.

The fit to NGC 7023 is initially set using the 23 most abundant PAHs, which constitute 95% of the fit. The remaining 10 are used to fill in the gaps of the profile of the 7.7 $\mu$m band and to fit the 8.6 $\mu$m feature. Using the first 25 most abundant PAHs —which contribute 96.8% (uid = 128–181 in Table 2.3)— the fit is completely set. The remaining 8 PAHs are used only to fill in minor details in the 6–9 $\mu$m range, since their spectra is mainly dominated by a few features in that wavelength region. We can affirm then, that the first 25 most abundant PAHs listed in Table 2.3 are in fact the important ones. Out of these, 8 are non-radical and contribute 43% to the total abundance of the fit. The last 8 PAHs only contribute 3.2%, and as such do not have a large effect on the ratios listed in Table 2.4.

Inspection of Table 2.4 shows that the mixture of *base-run* PAHs is mostly composed of small PAHs ($20 < N_c < 50$), adding up to a contribution of 68% versus the 32% abundance from large PAHs. Figure 2.6 shows the *base run* PAH size distribution in terms of the number of carbon atoms. Even though the PAHdb lacks large PAHs, the 7 PAHs having $50 < N_c < 70$ in the *base run* contribute 25% to the total abundance of PAHs in the fit. This is on average comparable to the abundance per PAH contributed by the smaller species. This may be pointing out the importance of medium sized PAHs having $50 < N_c < 70$. Larger PAHs contribute 7%, where the largest PAH used in the fit is $C_{170}H_{32}^{-}$ —at only 0.5% abundance—and is used to fill the profile of the 7.7 $\mu$m band due to its strong emission at 7.9 $\mu$m.

In terms of charge, the *base-run* set has neutral PAHs contributing 48% to the total abundance. *Base run* cationic species consist of mostly singly charged PAHs (3 dications contribute at a 5.6% level, while trications do not show up in any of the fits). The total input from cations is 26%, equal to that of anionic species. As mentioned above, anions are likely

Table 2.4: Results Derived From the Base Run Fit to the Features+Plateaus Spectra of NGC 7023, NGC 2023 and NGC 1333. See 2.5.1 for details.

| | NGC 7023 NW | NGC 2023 | NGC 1333 |
|---|---|---|---|
| **Fit** | | | |
| Average Photon Energy (eV) | 7.0 | 8.1 | 6.2 |
| Eucledian Norm* | 2.1 | 1.4 | 0.3 |
| Number of PAHs Used | 33 | 31 | 36 |
| **Size**** | | | |
| $x_{N_c<50}/x_{N_c>50}$ | 2.12 | 1.74 | 2.06 |
| **Ionization State**** | | | |
| $x_{PAH^+}/x_{PAH^0}$ | 0.42 | 0.45 | 0.38 |
| $x_{PAH^{+/++}}/x_{PAH^0}$ | 0.53 | 0.61 | 0.49 |
| $x_{PAH^-}/x_{PAH^0}$ | 0.53 | 0.59 | 0.51 |
| **Composition**** | | | |
| $x_{PANH}/x_{PAH}$ | 0.19 | 0.19 | 0.20 |
| **Structure** | | | |
| $n_{duo}/n_{solo}$ | 2.16 | 1.96 | 2.32 |
| $n_{trio}/n_{duo}$ | 0.24 | 0.22 | 0.23 |
| $n_{quartet}/n_{solo}$ | 0.13 | 0.14 | 0.05 |
| **Shape (%)** | | | |
| Compact Pericondensed (incl. 5–7) | 58.0 | 60.5 | 60.8 |
| Pericondensed With Edges (incl. 5–7) | 9.9 | 7.8 | 12.6 |
| Unbranched Catacondensed | 5.0 | 5.4 | 1.7 |
| Branched Catacondensed | 8.2 | 9.9 | 6.7 |
| Total contribution from PAHs with SW Defects | 24.6 | 25.5 | 27.3 |
| **Total contribution Pericondensed** | 67.8 | 68.3 | 73.4 |
| **Total contribution Catacondensed** | 13.3 | 15.3 | 8.4 |
| **Total contribution Irregular** | 16.0 | 13.2 | 15.8 |
| **Total contribution Completely Dehydrogenated** | 2.9 | 3.2 | 2.4 |

* The Eucledian Norm is defined as the square root of the residual sum of squares between the observed spectrum and the corresponding fit. ** All ratios are expressed in terms of the abundances of each species $x$. PAHs with $N_c < 50$ carbon atoms are considered to be small, while PAHs with $N_c > 50$ carbon atoms are considered to be large PAHs. In terms of ionization states, $PAH^0$ refers to neutral species; $PAH^{+/++}$ refers to all positively ionized PAHs; $PAH^+$ refers to only singly positively ionized PAHs; and $PAH^-$ refers to anionic species (PAHdb only contains singly negatively ionized PAHs). In terms of composition, $x_{PANH}/x_{PAH}$ refers to the abundance ratio of nitrogenated species relative to pure (carbon and hydrogen) PAHs. Hydrogen adjacency ratios are given in terms of the number of solo ($n_{solo}$), duo ($n_{duo}$), trio ($n_{trio}$) and quartet hydrogens ($n_{quartet}$), i.e. number of adjacent hydrogens attached to the same aromatic ring.

very overestimated because they are used to fill in for anharmonic red wings. Among the anions, the largest contribution from an anion is given by the second most abundant PAH: the PAH with *SW defects*, $C_{66}H_{20}^-$. This class of PAHs is used to fit the plateaus underneath the PAH bands (presumably because the *SW defect* only slightly perturbs the vibrational modes), and also to fit the 6.2 $\mu$m band (see more in the Appendix). If we perform the *base run* fit without considering any PAH with *SW defects*, we do get good quality fits where the contribution from Stone-Wales PAHs is replaced by increasing the fraction of PANHs (from 19% to 43% compared to pure PAHs) and small cationic species of slightly more irregular

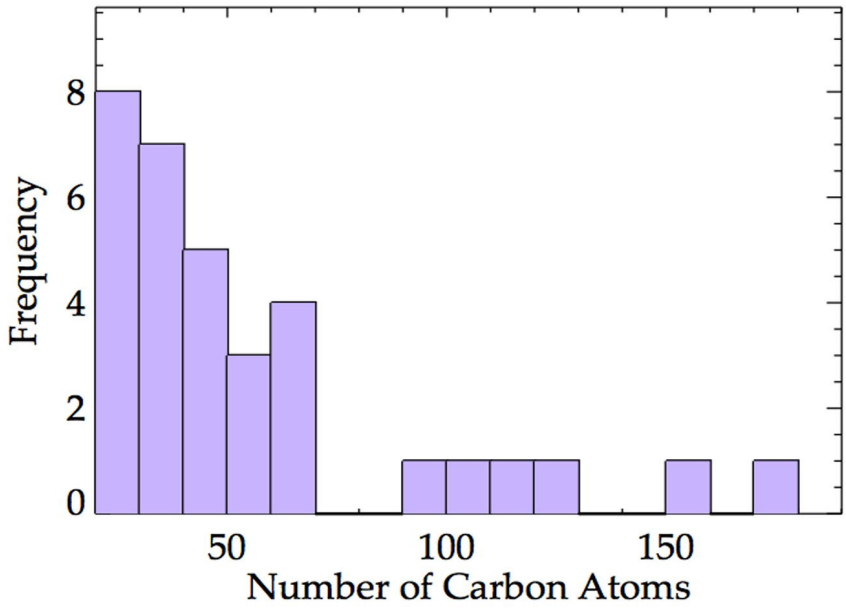


Figure 2.6: *Base run* PAH size distribution. Small PAHs having $20 < N_c < 50$ carbon atoms contribute 68% to the total abundance of PAHs in the fit to NGC 7023. Among the large PAHs, those having $50 < N_c < 70$ carbon atoms contribute 25%, while larger PAHs contribute 7% (see also Table 2.3).

structures (from $x_{\mathrm{PAH}^{+/++}}/x_{\mathrm{PAH}^0} = 0.53$ to 0.80). The contribution from anions is then only 10%. In fact, if we perform the fits without allowing any anions, we get similar results (e.g., PANHs contribute 30% and $x_{\mathrm{PAH}^{+/++}}/x_{\mathrm{PAH}^0} = 0.99$) without diminishing the quality of the fit. Thus the 26% contribution from anionic species should be considered as an upper limit.

Other minor inputs include completely dehydrogenated PAHs, which contribute only 3%. The spectra of completely dehydrogenated PAHs have, in general, very few salient features, and as such their spectra are used to fill in gaps at specific wavelengths in the 6–9 $\mu$m region.

Concerning the structure of *base-run* PAHs, Table 2.4 shows the PAHs are mostly compact and pericondensed in shape. Catacondensed PAHs contribute at a $\sim$10% level to the total abundance of PAHs in the *base run*, while irregular-shaped PAHs contribute at 15–20% level. The actual structure of the irregular-shaped PAHs is that of pericondensed PAHs with sharp edges and bay regions (e.g., see Figure 2.3). There are only 37 catacondensed PAHs in the initial pool of 292 PAHs. Test runs show that the observed spectra cannot be fitted well using only catacondensed PAHs, as the species included in the database lack strong 6.2 and 11.3 $\mu$m bands, a general characteristic of catacondensed species. In general, catacondensed PAHs will have weak solo out-of-plane C-H bending modes compared to duo and trio out-of-plane modes and hence, even if the database were more complete in terms of catacondensed PAHs, they would not be selected as an important component of the interstellar PAH family contributing to these spectra (Hony et al. 2001).

### 2.5.2. Degeneracy

The *base run* fit is subjected to a certain degree of degeneracy as classes rather than specific molecules are probed. To examine this degeneracy further, we proceeded to fit iteratively the observed spectrum of NGC 7023 using the *base run* condition, but removing all PAHs used in the previous fit each time. The fitting procedure was then allowed to use any of the PAHs remaining after each iteration that satisfied the criteria defined in 2.4. The results are summarized in Figure 2.7 in terms of the total number of different PAHs used in the fits, and the variation of ratios after each iteration. Figure 2.8 shows the first 4 fits. Here we clearly see that the fit gets significantly worse after 2 iterations, and the ratios vary considerably from one iteration to the other. Up until now, it has been recognized that random mixtures of PAHs can reproduce the general shape of the PAH emission spectra observed in different astronomical objects (Rosenberg et al. 2014). Here our exercise shows that even though completely different sets of PAHs can indeed produce the general shape of the PAH emission spectra, they cannot reproduce the spectrum in detail.

Naturally, the number of different sets that could reproduce the observed spectrum at a given level of detail is related to the incompleteness of PAHdb. Despite this, our results highlight that there is a preferred set of PAHs. The fitting procedure chooses the PAHs with bands at the precise, observed wavelengths. Once it runs out of these PAHs, it tries to reproduce the peak positions by combining different PAH spectra. This point is already reached at the first iteration, which reflects the intrinsic, subtle variations in the PAH spectra.

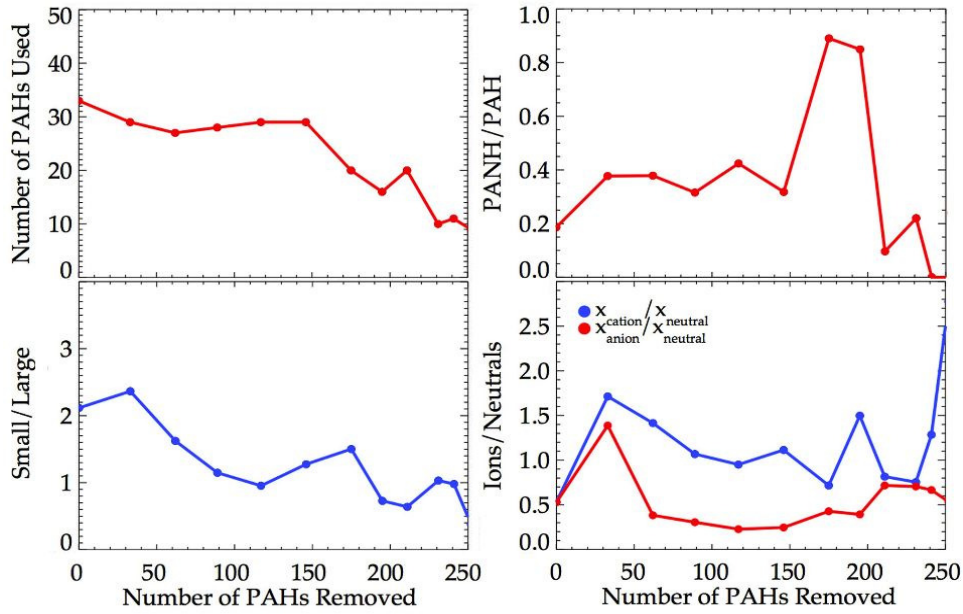


Figure 2.7: Results derived from the fits to the spectrum of NGC 7023 after sequentially removing all chosen PAHs after each iteration. The variation of composition, size and charge ratios are shown together with the number of PAHs used and removed after each iteration. The results are shown only for the first 10 iterations (241 PAHs removed from the initial pool). As shown from these plots, as we remove more PAHs, the ratios vary considerably from one iteration to the other.

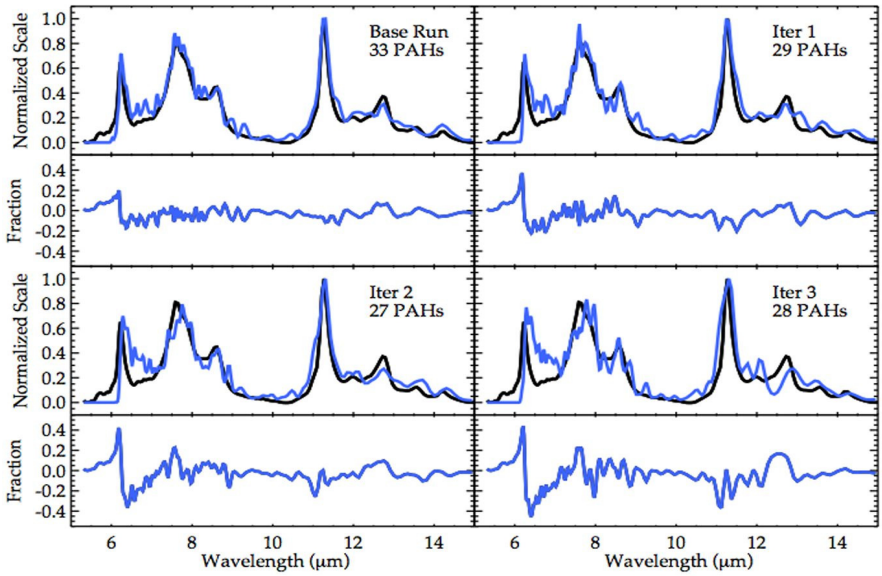


Figure 2.8: Fits to the spectrum of NGC7023 obtained after sequentially removing the entire set of PAHs used in the previous iteration. The first fit corresponds to the actual *base run*. All spectra have been normalized to the peak intensity of the 11.3$\mu$m feature. The observed spectrum is shown in black, while the fits are shown in blue. Also shown is the difference between each normalized fit and the observed normalized spectrum. Out of a pool of 292-33 PAHs, the first iteration uses 29 and the Eucledian norm is already increased by ~40% (right top panel). The second and third iterations are shown in the bottom panels. The third iteration is still be able to reproduce the overall shape of the observed spectrum, but fails in the details. At the third iteration the Eucledian norm has already exceeded that obtained in the *base run* by more than a 100%.

We can study the robustness of this last statement by performing the same exercise, but removing only the most abundant PAH each time. Figure 2.9 shows the number of PAHs used in each fit, and the contribution from *base-run* PAHs that are used after each iteration. As observed from both panels, the fits always use *base-run* PAHs to some degree. Also the fitting procedure uses a relatively steady number of PAHs to fit the spectrum, and the abundance of the most relevant PAH is at a 10% level for all runs.

Regarding the quality of the fits, Figure 2.10 shows the *base run* together with the fits after the removal of 10, 20 and 30 PAHs. As we remove an increasing number of PAHs, the fit has more trouble in reproducing the observations in detail, e.g., *problematic regions* get worse, and the fits have more difficulty reproducing the position and profile of the main PAH bands. The Eucledian norm increases by 23, 31 and 50% when we remove 10, 20 and 30 PAHs, respectively. Although this is a rather gradual variation, the Eucledian norm increases more rapidly from the $20^{th}$ iteration on. Figure 2.11 shows how the size, charge, structure and composition ratios vary throughout the first 30 iterations. From these values we can estimate average ratios for the first 20 fits. These are shown in Table 2.5 and appear to be consistent with the values presented in Table 2.4. Standard deviations represent variations of less than 30% for most ratios. The ratios that vary > 30% correspond to the fraction of PANHs relative to pure carbon PAHs, number fraction of quartet to solo-hydrogens, and the contribution of unbranched catacondensed PAHs.

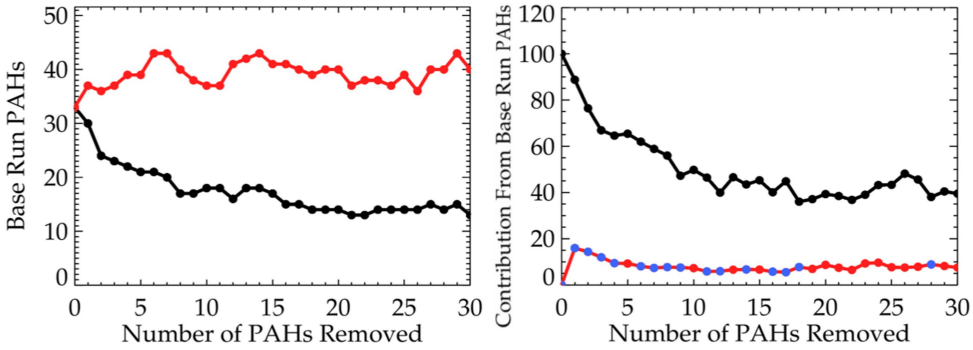


Figure 2.9: *Left panel.* Total number of different PAHs used in the fit to the *Features+Plateaus* spectrum of NGC 7023 after each iteration (in red). The black dots refer to the number of PAHs from the initial *base run* that are used in each iteration, e.g., the $0^{th}$ iteration corresponds to the actual *base run* fit where the 33 PAHs listed in Table 2.3 are used. *Right panel.* Contribution in relative abundance of the PAHs from the initial *base run* that are used after each iteration (in black), e.g., at the $0^{th}$ iteration *base-run* PAHs contribute in a 100% to the fit. Red dots refer to the most abundant PAH from the previous iteration that is removed each time. Blue dots indicate whenever the most relevant PAH removed was a *base-run* one, e.g., the first PAH removed is the most abundant one in the *base run* contributing in 16.0% as shown in Table 2.3.

From Figure 2.9 we notice that, as we remove the most abundant PAHs of each fit —which are most of the time *base-run* PAHs (see blue dots in Figure 2.9)— the fitting procedure uses different subsets of the remaining *base-run* PAHs to constitute the bulk of the fits. Each removed PAH is not replaced by another single new PAH, but by increasing the abundance of *base-run* PAHs, and adding a lower abundance of new PAHs to fill in the details of the spectrum. Figure 2.12 shows the coadded spectra of the *base-run* PAHs that have been removed in the first 20 iterations at their initial abundances derived in the *base run*. These 14 PAHs contributed a 68.4% abundance to the *base run* fit. These PAHs are mainly responsible for the strongest bands in the observed spectrum (e.g, 11.3 $\mu$m band).

Table 2.5: Average Size, Charge, Structure and Composition Ratios for the First 20 Iterations

| Small/Large | $x_{cation}/x_{neutral}$ | $x_{anion}/x_{neutral}$ | $x_{PANH}/x_{PAH}$ | $n_{duo}/n_{solo}$ | $n_{trio}/n_{duo}$ | $n_{quartet}/n_{solo}$ |
|---|---|---|---|---|---|---|
| 1.93±0.53 | 0.97±0.28 | 0.48±0.12 | 0.25±0.08 | 2.01±0.21 | 0.23±0.05 | 0.31±0.13 |
| Structure (Average contributions in %)[a] | | | | | | |
| Compact | With Edges | 5–7 | Branched | Unbranched | Irregular | Dehydrogenated |
| 53.98±4.37 | 11.06±4.46 | 15.58±4.24 | 11.83±1.77 | 9.63±4.09 | 8.85± 4.98 | 4.65±0.65 |

[a] See Figure 2.3 for the definitions of these structures.

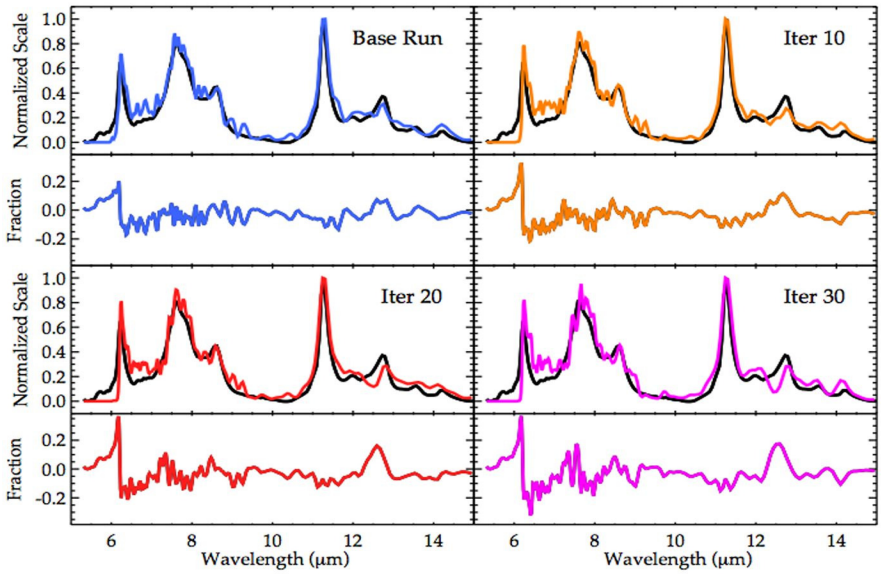


Figure 2.10: Fits to the spectrum of NGC7023 after removing 10, 20 and 30 PAHs compared to the *base run*. All spectra have been normalized to the peak intensity of the 11.3$\mu$m feature. The observed spectrum is shown in black, while the *base run* is shown in blue and the fits after the removal of 10, 20 and 30 PAHs are shown in the colors of each panel. Also shown is the difference between each normalized fit and the observed normalized spectrum. This figure shows that the quality of the fits decreases as we remove a larger number of PAHs, showing problems in matching band peak positions and the *problematic regions* explained in 2.5.1.

On the other hand, the 14 *base-run* PAHs used at the $20^{th}$ iteration contributed only 27.7% to the *base run* fit, but at the $20^{th}$ iteration they make up almost 40% of the total abundance of PAHs in the fit. In this iteration, the removed PAHs are replaced by comparable species. However, those do not reproduce the observed C-H out-of-plane bending bands to the same degree, as the quality of the fit at the $20^{th}$ iteration is less than that for the *base run*.

In summary, *base-run* PAHs appear to be the preferred set in order to reproduce the observations in detail. Nevertheless, as long as we are not concerned with a very detailed fit, the spectra of the PAHs in PAHdb are highly degenerate as, up to a point, any single PAH can be replaced —although not by a single other PAH— and the resulting spectrum is similar. However, it is not possible to produce identical fits.

## 2.6. Discussion

The results showed that, within the limits of the database, the *base-run* PAHs are the preferred set of PAHs to match the observations. Going back to the observations themselves, it is important to determine if variation in the distribution of relative abundances of *base-run* PAHs (see Table 2.3) can account for the observed differences between the three RNe. To address this question, we first performed a Monte Carlo experiment. This is then followed by a discussion on the effects of the incompleteness of the database, and the

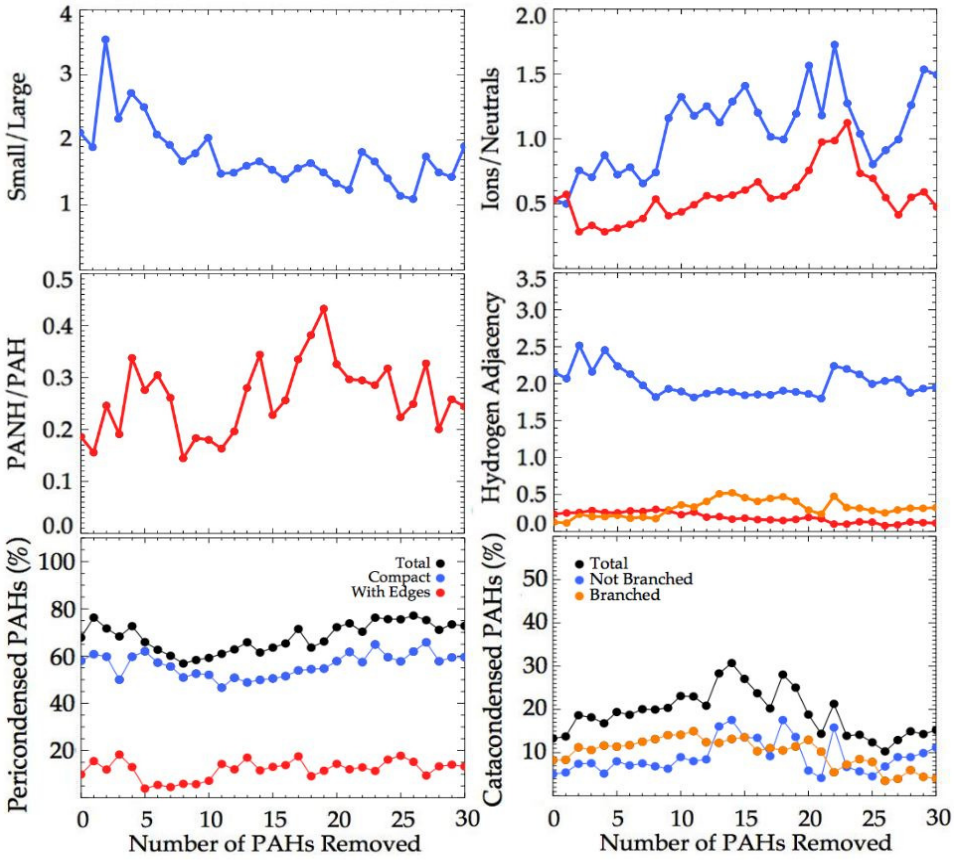


Figure 2.11: Size, Charge, Structure and Composition Ratios derived from the fits to the spectrum of NGC 7023. The results are shown only for the first 30 iterations. *Top* and *middle panels* show the ratios in terms of abundances. The bottom panels refer to the abundance contribution of PAHs classified according to their structure. The *left panel* shows the contribution from pericondensed PAHs (including PAHs with 5–7 ring *SW defects*), while the *right panel* shows the contribution from catacondensed PAHs. Irregular-shaped PAHs are not shown in these plots but tend to contribute at the 15% level, being mostly pericondensed in shape with few sharp edges.

limitations of the applied emission model on our results. Next the *grandPAH* hypothesis is outlined and, lastly, the concept of *grandPAHs* is applied to the spatial evolution of PAHs within NGC 7023.

### 2.6.1. Monte Carlo Experiment

We performed a Monte Carlo analysis on the relative abundances of the *base-run* PAHs derived from the fit to the spectrum of NGC 7023. Each PAH relative abundance was varied according to a Gaussian distribution of 5 000 random numbers around a mean given by the relative abundance derived from the *base-run* (listed in Table 2.3). The width of each Gaussian distribution represented the variation of the relative abundances as a certain percentage of the mean. All resultant spectra were then averaged (Figure 2.13).

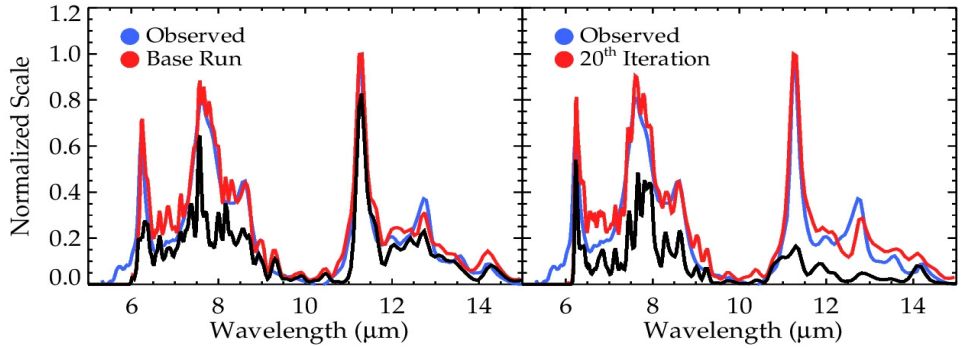


Figure 2.12: *Left panel.* Coadded spectra of the 14 *base-run* PAHs that have been removed by the time we perform the $20^{th}$ iteration (black curve). The spectra have been coadded using their respective contributions to the *base-run* fit. Also shown are the observed spectrum of NGC 7023 plotted in blue, and the *base run* fit which is shown in red. The removed *base-run* PAHs contribute greatly to the observed flux of the most salient bands, especially in the 10–15 $\mu$m region. *Right panel.* Spectra of the 14 *base-run* PAHs used in the $20^{th}$ iteration. The spectra have been stacked according to their contribution to the fit at the $20^{th}$ iteration (black curve). Also shown are the observed spectrum of NGC 7023 plotted in blue, and the fit at the $20^{th}$ iteration in red. As observed here, the coadded spectra fill in the strong bands at 5–9 $\mu$m, while the new PAHs are used to fit the long wavelength region which is not properly fitted as illustrated in Figure 2.10.

The results show that only a modest variation on the *base-run* relative abundances is enough to account for the small differences observed between the spectra of the three PDRs. The relative abundances of *base-run* PAHs can change up to 20% to account for the small differences observed between NGC 1333 and NGC 7023, and around 30% to explain the differences between NGC 2023 and NGC 1333.

We recognize that the derived percentage variation allowed depends largely on the quality of the fit in the *problematic regions* (see section 2.5.1) and hence, these variations are uncertain. However, we stress that the variation in the abundances allowed by the observed differences between the three RNe spectra are significantly less than the variations in the abundances of the PAHs in the *base run* (i.e., ranging from 16 to 3% for the first 10 PAHs in the *base run*), and this we consider a robust result. Taking this into account, it is even more striking to have such similar PAH emission at the studied locations of the three PDRs.

### 2.6.2. Limitations

Given that we focused on studying the fits at a detailed level, it is important to explore what determines how much detail we can go into when analyzing our results. Here several things come into play: the spectroscopic resolution of the Spitzer-IRS SL data, the completeness of PAHdb, and the calculation of PAH emission spectra. The resolution of our observed spectra does not allow one to discriminate between the A, B, C classifications of the 6.2 $\mu$m feature, and smears out the details in the 7.7 $\mu$m feature. We have already discussed the completeness of PAHdb in terms of the *problematic regions* in the fits. Concerning the PAH emission spectra, the FWHM and shift of the bands, the assumed band profile, and the emission model play a determinant role when studying the results of the fits.

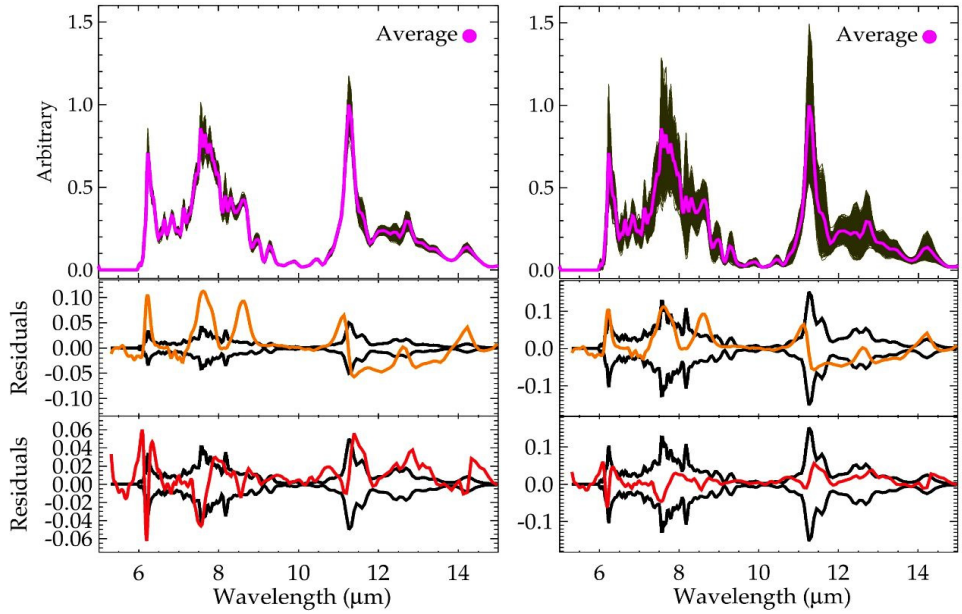


Figure 2.13: Monte Carlo analysis varying *base-run* relative abundances. *Top panels:* Average spectra obtained by varying the *base-run* relative abundances up to 10% (*left panel*) and 30% (*right panel*). *Bottom panels:* Comparison between the standard deviation of the averaged spectrum ($\pm 1\sigma$ shown in black) and the observed differences between the spectrum of NGC 7023 and that of NGC 2023 (shown in orange) and NGC 1333 (shown in red). Variations of 20–30% are enough to account for the observed differences between the spectra of the 3 PDRs.

Both the widening and shift of the bands are temperature, mode and molecule specific (Joblin et al. 1995; Pech et al. 2002; Oomens et al. 2003). Regarding the width of the bands, experiments have only been performed on a handful of small PAHs, and thus a constant value is assumed as a first approximation. Throughout this work we have adopted a FWHM = 15 $cm^{-1}$ using Gaussian profiles for all bands. Adopting the wavelength dependent FWHM of the bands as proposed in Bauschlicher et al. (2008) (see Appendix for details), we find that both the quality of the fit and the class ratios are actually similar to those of the *base run*. The main difference is that by using different band widths, the fit uses more PAHs than in the *base run* (44 PAHs against 33). It increases the fraction of nitrogenated PAHs (from 19% to 26%) and cationic species ($x_{PAH^{+/++}}/x_{PAH^0}$ = 0.53 to 0.84), by decreasing the contribution from neutrals and anions to 41% and 24%, respectively. Still the PAHs that contribute the most are *base-run* ones (30 out of the 44 PAHs), making up for 85% of the total abundance of PAHs in the fit. The largest contribution from one of the new PAHs is of 3.5% only. The shift of the bands are related to anharmonicities which are currently not well-understood and thus, we have used a single value as a first approximation. A further analysis on this is beyond the scope of this work.

As explained in 2.4.1 we assumed Gaussian profiles for all bands. Using Lorentzian profiles instead (see Appendix), we again obtain results quite similar to the original *base run* fit, e.g., the most abundant species are the same for both fits. The largest difference is also in the number of PAHs used to fit the spectrum. When using Lorentzian profiles only

26 PAHs are required for a good fit, which relates to the fact that with a Lorentzian profile, the same PAHs that produce the narrow features also produce much of the plateaus, given the extensive wings of Lorentzian profiles.

With respect to the PAH emission model, the only physical condition we have taken into account is the strength of the radiation field as emitted by the exciting star. Our approach does not consider ionization balance, and we have not used any constraint regarding reactions of formation/destruction of PAHs when fitting the observed spectra. A further analysis on these is encouraged and will be treated in a future work.

### 2.6.3. The Local Physical Environment

Given the similarity in the PAH emission spectra, we expect physical conditions also to be similar at these spots. Indeed all spectra show a similar 6.2/11.3 ratio. This ratio is known to be driven by ionization. Inspection of Table 2.2 shows the ionization parameter $\gamma$ for NGC 7023 is $6.5\times10^4$. Using the upper limit for $G_0$ published in Okada et al. (2013), $\gamma$ increases by a factor of 3. NGC 2023 on the other hand has a $\gamma$ value of $3.4\times10^4$. The interclump medium in this case has a $\gamma$ which is a factor 4 larger. However we expect that the PDR emission is dominated by the clump. The ionization parameter for NGC 1333 is between that of NGC 7023 and NGC 2023, $4.5\times10^4$, but overall we see that the ionization parameter varies within a factor of 2 between the three PDRs, which is expected to fall within the uncertainties in the estimated parameters. This agrees with the fact that all fits lead to similar $x_{\mathrm{PAH}^{+/++}}/x_{\mathrm{PAH}^0}$ ratios, where neutral PAHs dominate the spectra contributing $\sim 50\%$, while the input from cationic species accounts for 25% of the total abundance of PAHs in the fits (or even larger given that the contribution from anionic species should be considered as an upper limit). Even though we did not take ionization balance into account, our results agree with theoretical calculations for circumcoronene (Tielens 2005). According to this, a variation of a factor of 2 in $\gamma$ would be translated in a factor of 1.4 in the ionization fraction, and for $\gamma$ values of a few $10^4$, we should indeed expect neutral and cationic species to be dominant, with a negligible contribution ($< 10\%$) from anions and doubly cationic species.

Aside from ionization, the chemical state of the PAH population is also a reflection of the local physical conditions, and of the history. We can discuss the chemical state of PAHs in terms of the 12.7/11.3 and 8.6/6.2 ratios. The 12.7/11.3 is often considered a measure of the molecular edge structure, while the 8.6/6.2 ratio is an indicator of the size of compact symmetric PAHs (Ricca et al. 2012). Both ratios vary widely within each source. However they are very similar at the bright spots studied here. Even the much weaker 12.0, 13.5 and 14.2 $\mu$m bands (which measure the presence of duo/trio modes) have the same intensity among the three locations. Likewise, while all (cationic) pericondensed PAHs show strong bands in the 7.6–8.0 $\mu$m range, the 8.6 $\mu$m band is characteristic for highly condensed, symmetric PAHs such as the pyrene, coronene or ovalene family (Bauschlicher et al. 2009; Ricca et al. 2012).

In addition, even though we did not analyze the 15–18 $\mu$m emission with PAHdb, we would like to point out the similarity between all three spectra as observed from Figure 2.14. This similarity is not only in terms of the presence of features, but also their relative intensities. The spectra only differ in the $H_2$ 17.0 $\mu$m line emission, which is still $< 20\%$. The 15–18 $\mu$m wavelength range is expected to be related to C-skeletal modes and/or the

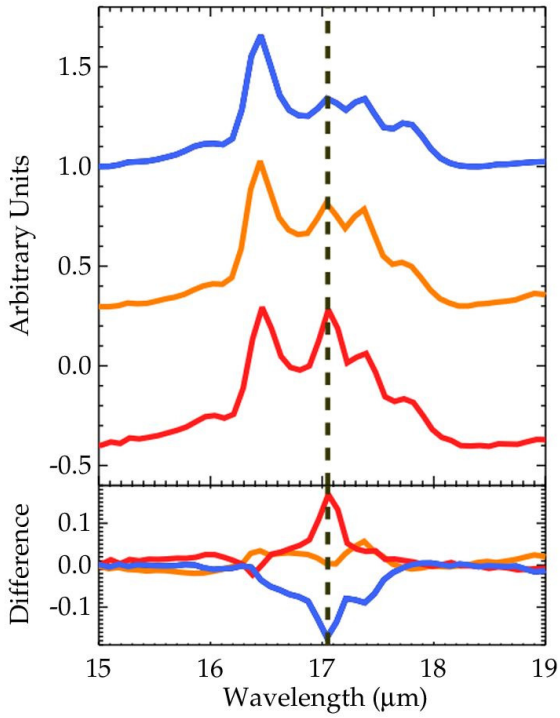


Figure 2.14: Continuum-subtracted 15–19 $\mu$m spectra of the brightest locations in NGC 7023, NGC 2023 and NGC 1333 (*top panel*). The *bottom panel* shows the difference between each normalized spectrum with the average of all three spectra using the same color scheme. For this wavelength range the continuum has been defined fitting a spline function to the anchor points listed in 2.2.3 plus an anchor point at 18.0 $\mu$m. Just as in the short wavelength region (Figure 2.2), the spectra show the same bands and very similar relative intensities. The largest difference is observed in the $H_2$ S(1) 17.0 $\mu$m line, where the spectra differ by about 20% (dashed line).

edge structure of PAHs, and therefore it is to some extent molecule specific. Inspection of PAHdb shows PAH spectra have a wide variety of features and relative intensities in this wavelength range. However in the spots studied here, we see a remarkable similar emission from only few bands.

Hence, these examples illustrate clearly that the emitting PAH families have to be fairly similar in order to produce such highly similar spectra observed at these different locations.

### 2.6.4. GrandPAH Hypothesis

The prevalence of a single preferred subset of PAHs leads one to conjecture about the idea of a possible set of *grandPAHs*. As mentioned in the introduction, the concept of *grandPAHs* has been defined in the literature as a set of the most stable PAH species that can survive in the harsh conditions of the ISM (Tielens 2013). Here we now can examine the *grandPAH* hypothesis in more detail, and refine the concept for the case of RNe.

Our concept of *grandPAHs* relies on the following six points:

1) The spectroscopic similarity between the three observed spectra, even in the smallest details (Figures 2.2 and 2.14).

2) The initial *base run* fits showed the same PAH subclass breakdown for the three spectra, revealing an insensitivity of the PAH emission to the shape of the radiation field (Table 2.4).

3) The degeneracy study that removed iteratively the whole fitted set, clearly showed that the set of *base-run* PAHs is the preferred set in order to reproduce the observations in detail (2.5.2).

4) The degeneracy study that removed iteratively the most abundant PAH also showed the same preferred set of *base-run* PAHs. It also hinted at the large diversity in PAH spectra available in PAHdb (2.5.2). For example, there it was shown that the most abundant PAHs are mainly chosen for having an intense 11.3$\mu$m band, that can fit the observed one with only 1.4 cm$^{-1}$ difference in peak positions. As more of these PAHs are removed from the pool, the fitting procedure finds it more difficult to fit this band, and we notice that —very rapidly— there are no more PAHs (either alone or a combination of them) that can fit the band in detail.

5) The Monte-Carlo analysis showed that subtle variations in the abundance distribution of the preferred set of PAHs can explain the observed minor variations between the three observed spectra (2.6.1).

6) Estimates of the ionization parameter at the three locations show they are similar, varying by only a factor of 2 (2.6.3).

Points 1–4 indicate that, within the limits of the database and Spitzer spectral resolution, there is one set of PAHs that explains the observations best. Point 5 shows that the subtle variations between the three spectra can be explained with only the one set of PAHs. Lastly, point 6 supports the fact that the local physical environment would be driving the PAH population to the *grandPAHs*.

It is important to emphasize that we are not saying the *base-run* set of PAHs is the actual *grandPAH* family. Instead, we are stating that the available data implies that a limited number of compact, highly symmetric PAHs dominate the interstellar PAH family at the brightest spots of RNe, and that they share the *base run* characteristics (e.g., the ratios shown in Table 2.4).

### 2.6.5. GrandPAH Evolutionary Scenario

Since NGC 7023 NW is an edge-on PDR, and the PAH emission has been extensively studied throughout the entire nebula, we can take NGC 7023 as a reference to analyze what is happening at these bright spots.

The position studied in this work is located along the brightest rim of NGC 7023, 40" north-west of the exciting star. Our location falls in the peak emission of the filament observed in Extended Red Emission, and it also coincides with the bulk of the [CII] emission

(Berné et al. 2008). Regarding molecular hydrogen, the peak of the PAH emission is slightly offset from where the $H_2$ peak is observed, being closer to the star and at the limit where the ortho-to-para ratio $R_{OP}$ decreases from the LTE value (Fleming et al. 2010; Sellgren et al. 2010). In fact the spectrum of the brightest spot does not show strong $H_2$ emission lines in the mid-IR range. Interestingly, this holds for all three PDRs (Figure 2.2).

Berné et al. (2007) performed a blind signal separation analysis on the spectral data cube of NGC 7023. Their analysis revealed that NGC 7023 shows a stratified structure where the PAH emission closer to the star is dominated by cationic species, while the PAH emission further away from the star is dominated by neutral PAHs. They also reported a third signal whose emission dominates deeper into the cold molecular cloud, and that they assigned to very-small-grains (VSG). This VSG emission disappears as the PAH emission dominated by neutral species becomes more important in the PDR front (see also Sellgren et al. 2010; Rosenberg et al. 2011). This was interpreted as a transformation process where VSGs are photo-evaporated, releasing free flying PAHs into space as they get destroyed due to the incoming UV radiation. According to this scheme, when VSGs are destroyed they release mostly neutral PAHs, and those PAHs close enough to the star become ionized/destroyed as a result of the intense radiation. Indeed in their maps, the location of the brightest mid-IR spot falls right at the peak of the signal dominated by neutral PAHs, neighboring the border where the VSG abundance decreases considerably, while the emission from neutral PAHs starts dominating the spectra, as we leave the molecular cloud going into the PDR region. Their suggestion that PAH emission is dominated by neutral PAHs agrees with our derived ratios as listed in Table 2.4. According to Berné & Tielens (2012) the brightest spot of the PDR is located where the abundance of PAHs starts decreasing, right at the edge of the transition zone between the beginning of the molecular cloud and the PDR. Boersma et al. (2013) shows that this is also where the relative contributions from the different PAH subclasses making up the PAH mixture start to change.

Within the interpretation given by Berné et al. (2007) and Berné & Tielens (2012), the brightest location of the PDR would be the place where the intense processing of the PAHs starts; where PAHs are being released from the VSGs, ice mantles and other PAH reservoirs inhabiting the dense molecular cloud. The free flying PAHs will quickly lock into the ionization balance since this process is much more quickly established than the evaporation timescale of PAH clusters in PDRs. The released PAHs should also be (or should be further processed into) mainly small-to-medium size PAHs (30–50 carbon atoms), pericondensed in shape. The last figure of this chapter (page number 54) schematically shows where *grandPAHs* fall within the evolution of carbonaceous material in a RN such as NGC 7023. The figure shows the transformation the PAH population goes through from the molecular cloud (right side) to the region closest to the star (left side) based on what is known from NGC 7023. The bottom panel corresponds to a composite image of NGC 7023 from the star to the NW PDR. The three-color image has been built from combining PACS 70 $\mu$m (red), 6.2 $\mu$m (green; image courtesy O. Berné) and MIPS 24 $\mu$m (blue) images, and shows the brightest spot studied in our work (edge between the *PDR* and the *molecular cloud*).

In NGC 7023 it has been observed that there is a flow of material from the molecular cloud to the PDR, through the PDR front, into the cavity (Fuente et al. 1998). As the material flows through the molecular cloud to its surface and through the PDR front into the cavity, PAH clusters/VSGs and PAHs are exposed to a stronger radiation field, which induces a pronounced chemical evolution. Initially this will lead to a slow evaporation of PAHs from

PAH clusters/VSGs (right side of the figure). There PAHs are freed when they meet the radiation from the star for the first time. These newly freed PAHs will be further processed and become the population of *grandPAHs*: a unique mixture of the most stable PAHs. Initially this population would be dominated by neutral PAHs, of small-to-medium sizes and compact pericondensed structure. Those *grandPAHs* that get close enough to the star will then become ionized, dehydrogenated and eventually destroyed. Under an even stronger UV radiation field (the closest region to the star) these ionized and fragmented PAHs will end up in the most stable forms of fullerenes.

We surmise then that at the brightest spots of RNe, the PAHs are first exposed to the strong radiation field of the illuminating stars, and this converts the members of the PAH family to the most stable PAH species, where side groups as well as dangling rings are photochemically eroded. We have seen that $G_0$, $T_{gas}$ and $n_H$ vary between the three nebulae: $G_0$ varies by a factor of 5–6, $T_{gas}$ varies by a factor of 3–4, and $n_H$ varies from 4 000 to $10^5$ cm$^{-3}$. However the ionization parameter varies by only a factor of 2. Thus, it is tempting to link the chemical variations to $\gamma$ and/or $G_0/n_H$. This last variable has been identified as the driving force for the PAH-to-fullerene conversion (Berné & Tielens 2012), and it has also been suggested to determine the hydrogenation state of PAHs as long as multiphoton events are not important (Montillaud et al. 2013). Thus, it may also play a role in the PAH-to-*grandPAH* family conversion, as hydrogen has a much lower binding energy, and experiments show hydrogen loss occurs much more rapidly than $C_2H_2$ or $C_2$ loss (Ekern et al. 1998). In this view, the change in the ionization balance and the chemical conversion of PAHs to *grandPAHs* are both linked to $G_0/n_H$. This may be the underlying cause as to why the spectra of the bright spots studied here are so similar in their ionization and chemical character.

## 2.7. Summary and Conclusions

We analyzed the PAH emission observed in the Spitzer-IRS spectra of the brightest PDRs of three well-known different reflection nebulae: NGC 7023, NGC 2023 and NGC 1333. These locations are the brightest spots within the rims that delineate transition zones of the molecular cloud and the surroundings, as observed in the mid-IR. The three nebulae are illuminated by different stars; and overall the intensity of the UV radiation field, together with the gas density and temperature are known to be different between them. In terms of PAH emission, each one of them show variations in relative ratios and appearance of features when studied through spectral mapping. Despite all this, the mid-IR spectra at the brightest spots studied here show practically the same PAH emission.

In order to tackle this issue, we used the theoretical PAH spectra comprised within The NASA Ames PAH IR Spectroscopic Database, to fit the observations and analyze the derived PAH populations. The results of the fits led to remarkably similar PAH populations for all three spectra, representing a mixture of mostly neutral small PAHs contributing in $\sim 50\%$, while cationic and anionic species contribute 25% abundance each. Such input from anionic species is known to be overestimated since —given the PAHs within the database— anionic species are systematically used to reproduce the observed shift of PAH bands relative to the theoretical estimates. Contributions from nitrogenated and Stone-Wales species are $\lesssim 25\%$, and should also be taken cautiously given the characteristics and incompleteness of the database.

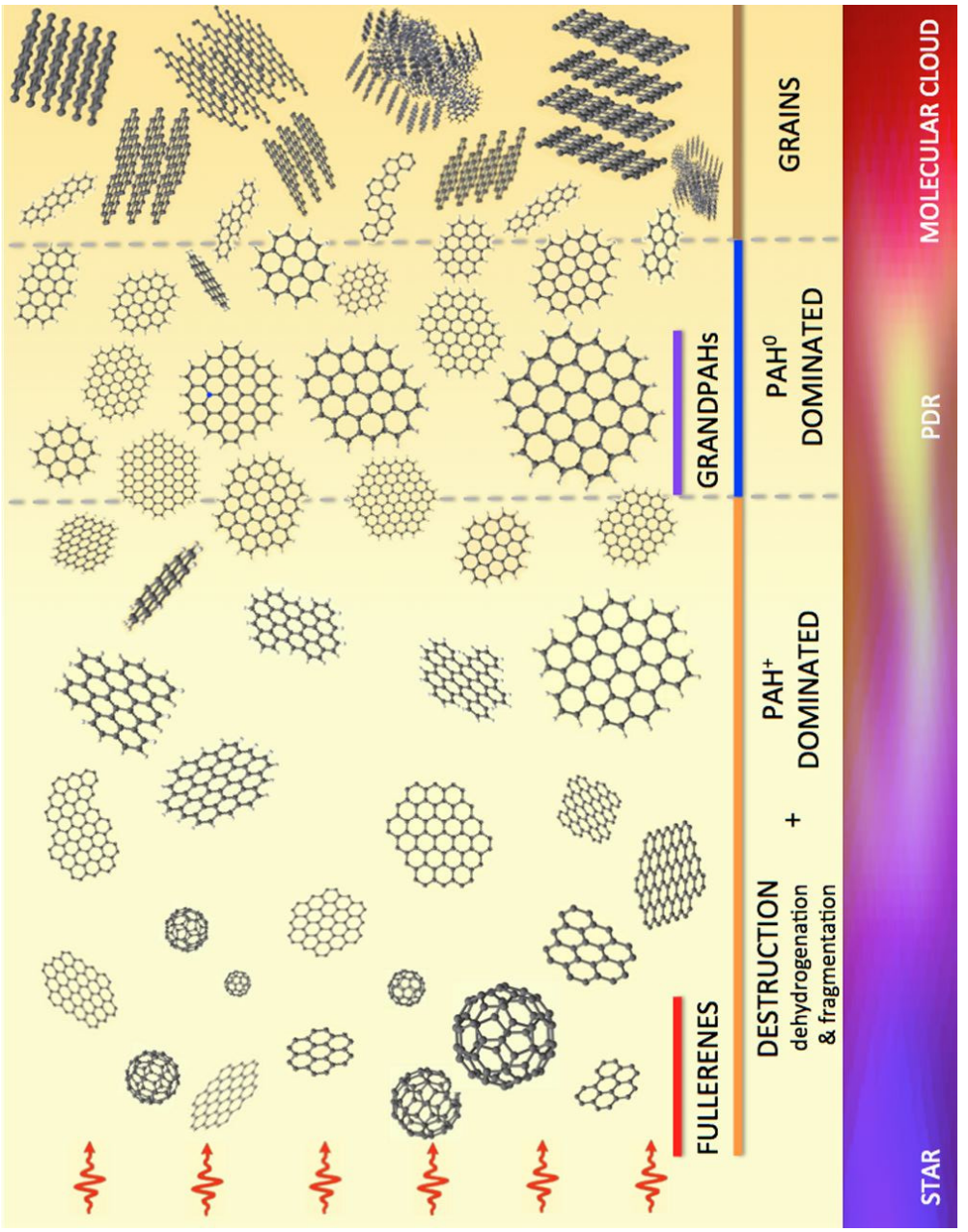
STAR
FULLERENES
DESTRUCTION
dehydrogenation
& fragmentation
+
PAH+
DOMINATED
GRANDPAHs
PAH0
DOMINATED
GRAINS
PDR
MOLECULAR CLOUD

The analysis on the degeneracy of the results showed that the properties of this set of PAHs are, indeed, necessary to reproduce the details of the observed PAH emission. In this sense, we conclude that not any random mixture of PAHs can fit the observations *in detail*. Furthermore, small variations in relative abundances can indeed produce differences in the spectra that are larger than what we observe between NGC 7023, NGC 2023 and NGC 1333. Thus, together with the fact that the three spectra show extremely similar ratios that are known to be related to the ionization and chemical state of the PAH population, we propose that PAH populations must be remarkably similar at these different lines-of-sight. As an explanation, we considered the concept of the *grandPAHs* as a unique mixture of PAHs that dominates the emission at the brightest spot of all three PDRs. Such a set of PAHs would be the result of extensive processing that takes place at these locations, and that does not depend on the histories nor the initial mixture of PAHs present in these nebulae. Even though this concept of *grandPAHs* has been presented in the literature before, our work constitutes the first attempt to test and draw specific conclusions regarding this hypothesis, given the current state of the PAH field.

We would like to emphasize that the set of PAHs derived from the fit is not the actual *grandPAH* family. Instead, our results point towards a limited number of compact (highly symmetric) PAHs dominating the interstellar PAH family at the brightest spots of the RNe studied here. We also propose that the *grandPAHs* would indeed share the properties and characteristics of the set of PAHs derived from our fits.

We recognize that the degree of degeneracy of our results depends on both Spitzer spectral resolution and how complete the database is. Perhaps, the more complete the database, the greater the degeneracy we would likely obtain. However the analysis on these three PDRs indicates that there is a preferred set of structures and sizes. Unfortunately we cannot assess their uniqueness, chemically, unless we put more constraints or study more spectra. PAH relative band intensities in the 5–15 $\mu$m region appear to be largely insensitive to variations of the radiation field, which is the only parameter we are considering when calculating each PAH emission spectrum. These uncertainties can be significantly tightened by the availability of fully resolved, complete 2.5–20 $\mu$m spectra.

We finally propose that the *grandPAH* population in RNe is the outcome of the intense processing of carbonaceous material at the transition interface between the PDR and the cold molecular cloud, where the PAH population (initially in the molecular cloud) faces the strong stellar radiation field for the first time. Further processing of the *grandPAH* population in regions closer to the exciting star would produce a large population of cationic species and irregular PAH structures, that under even more extreme conditions would stabilize into fullerene forms.

## Acknowledgements

Studies of interstellar PAHs at Leiden Observatory are supported through advanced ERC grant 246976 from the European Research Council, through a grant by the Dutch Science Agency, NWO, as part of the Dutch Astrochemistry Network, and through the Spinoza premie from the Dutch Science Agency, NWO. This work is based [in part] on observations made with the Spitzer Space Telescope, which is operated by the Jet Propulsion Laboratory, California Institute of Technology under a contract with NASA. CB and

LA gratefully acknowledge support from NASA's "Carbon in the Galaxy" consortium grant (NNH10ZDA001N) and NASA's Astrobiology; Astronomy and Physics Research and Analysis (APRA; NNX07AH02G) and Spitzer Space Telescope Support programs (50082). CB is grateful for an appointment at NASA's Ames Research Center through San José State University Research Foundation (NNX14AG80A).

# Bibliography

Aannestad, P. A., & Kenyon, S. J. 1979, ApJ, 230, 771
Alecian, E., Catala, C., Wade, G. A., et al. 2008, MNRAS, 385, 391
Ali-Haïmoud, Y. 2014, MNRAS, 437, 272
Allamandola, L. J., Tielens, A. G. G. M., & Barker, J. R. 1985, ApJ, 290, L25–L28
Allamandola, L. J., Hudgins, D. M., & Sandford, S. A. 1999, ApJ, 511, L115
Bakes E.L.O., Tielens A.G.G.M., Bauschlicher, Jr. C.W., 2001, ApJ, 556, 501
Barker, J. R., Allamandola, L. J., & Tielens, A. G. G. M. 1987, ApJ, 315, L61
Bauschlicher, C. W., Peeters, E., & Allamandola, L. J. 2008, ApJ, 678, 316
Bauschlicher, C. W., Peeters, E., & Allamandola, L. J. 2009, ApJ, 697, 311
Bauschlicher, C. W., Boersma, C., Ricca, A., et al. 2010, ApJS, 189, 341
Berné, O., Joblin, C., Deville, Y., et al. 2007, A&A, 469, 575
Berné, O., Joblin, C., Rapacioli, M., et al. 2008, A&A, 479, L41
Berné, O., Joblin, C., Mulas, G., Tielens, A. G. G. M., & Goicoechea, J. R. 2009, arXiv:0910.4069
Berné, O. & Tielens, A. G. G. M. 2012, Proc. of the National Academy of Science of the United States, 109, 401
Boersma, C., Mattioda, A. L., Bauschlicher, C. W., et al. 2009, ApJ, 690, 1208
Boersma, C., Bauschlicher, C. W., Allamandola, L. J., et al. 2010, A&A, 511, A32
Boersma, C., Rubin, R. H., & Allamandola, L. J. 2012, ApJ, 753, 168
Boersma, C., Bregman, J. D., & Allamandola, L. J. 2013, ApJ, 769, 117
Boersma C. et al., 2014, ApJS, 211, 8
Bregman, J., & Temi, P. 2005, ApJ, 621, 831
Cami, J. 2011, in EAS Publications Series, Vol. 46, PAHs and the Universe, ed. C. Joblin & A. G. G. M. Tielens (Cambridge: Cambridge Univ. Press), 117
Cardelli, J. A., Meyer, D. M., Jura, M., & Savage, B. D. 1996, ApJ, 467, 334
Chokshi, A., Tielens, A. G. G. M., Werner, M. W., & Castelaz, M. W. 1988, ApJ, 334, 803
Cook, D. J., & Saykally, R. J. 1998, ApJ, 493, 793
Crawford, M., Tielens, A., & Allamandola, L. 1985, ApJ, 293, L45
de Boer, K. S. 1983, A&A, 125, 258
Ekern, S. P., Marshall, A. G., Szczepanski, J., & Vala, M. 1998, J. Phys. Chem., 102, 3498
Fleming, B., France, K., Lupu, R. E., & McCandliss, S. R. 2010, ApJ, 725, 159
Fuente A., Martín-Pintado J., Rodríguez-Franco A., Moriarty-Schieven G.D., 1998, A&A 339, 575
Galliano, F., Madden, S. C., Tielens, A. G. G. M., Peeters, E., & Jones, A. P. 2008, ApJ, 679, 310
Galué, H. A. 2014, Chem. Sci., DOI: 10.1039/C4SC00890A
Hollenbach, D. R., Tielens, A. G. G. M. 1999, Rev. Mod. Phys., 71, 173
Hony, S., van Kerckhoven, C., Peeters, E., et al. 2001, A&A, 370, 1030
Houck, J.R., Roellig, T.L., van Cleve, J., et al. 2004, ApJS, 154, 18
Hudgins, D. M., Bauschlicher, C. W., & Allamandola, L. J. 2005, ApJ, 632, 316
Joblin, C., Boissel, P., Léger, A., d'Hendecourt, L., & Defourneau, D. 1995, A&A, 299, 835
Kurucz, R. L. 1993, VizieR Online Data Catalog, 6039, 0
Langhoff, S. R. 1996, J. Phys. Chem., 100, 2819
Lawson, C. L., & Hanson, R. J. 1974, Solving Least Squares Problems (Prentice-Hall Series in Automatic Computation; Englewood Cliffs, NJ: Prentice-Hall)
Léger, A. & Puget, J. L. 1984, A&A, 137, L5–L8
Li A., Draine B. T., 2001, ApJ, 550, L213
Markwardt, C. B. 2009, in Astronomical Society of the Pacific Conference Series, Vol. 411, Astronomical Data Analysis Software and Systems XVIII, ed. D. A. Bohlender, D. Durand, & P. Dowler, 251
Montillaud, J., Joblin, C., Toublanc, D. 2013, A&A, 552, A15
Mookerjea, B., Sandell, G., Jarrett, T. H., & McMullin, J. P. 2009, A&A, 507, 1485
Okada, Y., Pilleri, P., Berné, O., et al. 2013, A&A, 553, A2
Oomens, J., Tielens, A. G. G. M., Sartakov, B. G., von Helden, G., & Meijer, G. 2003, ApJ, 591, 968
Pech, C., Joblin, C., & Boissel, P. 2002, A&A, 388, 639
Peeters, E., Hony, S., Van Kerkhoven, C., Tielens, A. G. G. M., Allamandola, L. J., Hudgins, D. M., &

Bauschlicher, C. W. 2002, A&A, 390, 1089
Peeters, E., Tielens, A.G.G.M, Allamandola, L.J., & Wolfire, M.G. 2012, ApJ, 747, 44
Pilleri, P., Montillaud, J., Berné, O., & Joblin, C. 2012, A&A, 542, A69
Pino, T., Dartois, E., Cao, A.-T., et al. 2008, A&A, 490, 665
Purcell, E. M. 1976, ApJ, 206, 685
Ricca, A., Bauschlicher, C. W., Jr., Mattioda, A. L., Boersma, C., & Allamandola, L. J. 2010, ApJ, 709, 42
Ricca, A., Bauschlicher, C. W., Jr., & Allamandola, L. J. 2011, ApJ, 729, 94
Ricca, A., Bauschlicher, C. W., Jr., Boersma, C., Tielens, A. G. G. M., & Allamandola, L. J. 2012, ApJ, 754, 75
Rogers, C., Heyer, M. H., & Dewdney, P. E. 1995, ApJ, 442, 694
Rosenberg, M. J. F., Berné, O., Boersma, C., Allamandola, L. J., & Tielens, A. G. G. M. 2011, A&A, 532, A128
Rosenberg, M. J. F., Berné, O., Boersma, C. 2014, A&A, 566, 4
Schutte, W. A., Tielens, A. G. G. M., & Allamandola, L. J. 1993, ApJ, 415, 397
Sellgren, K., Uchida, K. I., & Werner, M. W. 2007, ApJ, 659, 1338
Sellgren, K., Werner, M. W., Ingalls, J. G., et al. 2010, ApJ, 722, L54
Sheffer, Y., Wolfire, M., Hollenbach, D. J., Kaufman, M. J., & Cordier, M. 2011, ApJ, 741, 45
Smith, J. D. T., Draine, B. T., Dale, D. A., et al. 2007, ApJ, 656, 770
Steiman-Cameron, T. Y., Haas, M. R., Tielens, A. G. G. M., & Burton, M. G. 1997, ApJ, 478, 261
Stein, S. E. 1978, J. Phys. Chem., 82, 566
Stone, A. J., & Wales, D. J. 1986, Chem. Phys. Lett., 128, 501
Tielens, A. G. G. M., & Hollenbach, D. 1985, ApJ, 291, 722
Tielens, A. G. G. M. 2005, The Physics and Chemistry of the Interstellar Medium (Cambridge: Cambridge Univ. Press)
Tielens, A. G. G. M. 2013, Rev. Mod. Phys., 85, 1021
Werner, M. W., Uchida, K. I., Sellgren, K., et al. 2004, ApJS, 154, 309
Werner, M. W., Sellgren, K., & Livingston, J. 2009, AAS Meeting Abstracts, 213, #412.15
Whitesides, R., & Frenklach, M. 2010, J. Phys. Chem. A., 114, 689
Young Owl, R. C., Meixner, M. M., Fong, D., Haas, M. R., Rudolph, A. L., & Tielens, A. G. G. M. 2002, ApJ, 578, 885
Yu, H., & Nyman, G. 2012, ApJ, 751, 3

## 2.A. Features+Plateaus versus Features-Only Spectra

As mentioned in 2.4, both the nature of the plateau carriers, and the intrinsic profile of PAH bands are unknown. Because of this we decided to base our results on *Features+Plateaus* spectra only. Here we briefly explore the results for *Features-Only* spectra.

Figure 2.15 shows the fit to the *Features-Only* spectrum of NGC 7023 using the *base run* condition presented in §2.4. The residuals of the fits in the *problematic regions* described in §2.5.1 are at a similar level as the differences shown in Figure 2.4 of the main text. The excess at $\sim$7 and 8 $\mu$m are partly related to the *problematic regions* inherent to the fits, and partly to the fact that when performing the spline decomposition we are also removing the emission that is attributed to the wings of the PAH bands, whose intrinsic profile is unknown.

Regardless of the quality of the fits, we can get useful information about the properties of the underlying PAH population. Table 2.6 lists the PAHs used in the fit. We see that the fitting procedure uses less PAHs than to fit the *Features+Plateaus* spectra (e.g., 25 against 33 in the case of NGC 7023). Out of the 25 PAHs used in the fit, 16 are also used in the fit to the *Features+Plateaus* spectrum of NGC 7023. These PAHs contribute in 68% and 60% to the total abundance of PAHs in the *Features-Only* and *Features+Plateaus* spectra, respectively.

Table 2.7 shows the class ratios of the sets of PAHs derived from the fits to the *Features-Only* spectra of NGC 7023, NGC 2023 and NGC 1333. Overall most ratios are consistent with the values derived for *Features+Plateaus* spectra. There is however an increase in the cation fraction, while the anionic fraction relative to neutrals decreases in $>50\%$. Part of this change is related to the fact that

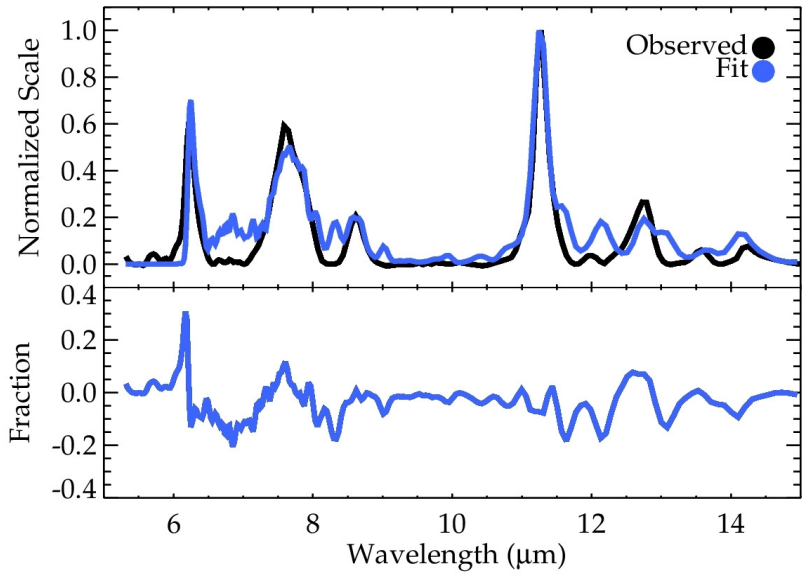


Figure 2.15: Base run fit to the *Features-Only* spectrum of the brightest location in NGC 7023. The spectra are shown in normalized scale. The figure also shows the difference between both normalized spectra. For NGC 7023 out of a pool of 292 PAHs, the fit ends up using 25 PAHs. Table 2.6 lists the PAHs used in this fit.

Table 2.6: Base-run PAHs derived from fit to NGC 7023 Features–Only spectrum

| Uid | Formula | Abundance (%) | $n_{solo}$ | $n_{duo}$ | $n_{trio}$ | $n_{quartet}$ | Structure |
|---|---|---|---|---|---|---|---|
| 620 | $C_{42}H_{16}$ | 14.5 | 4 | 12 | 0 | 0 | Pericondensed |
| 228 | $C_{23}H_{12}N^+$ | 13.0 | 0 | 12 | 0 | 0 | Pericondensed |
| 37 | $C_{54}H_{18}$ | 11.8 | 6 | 12 | 0 | 0 | Pericondensed |
| 11 | $C_{32}H^-_{14}$ | 7.0 | 2 | 12 | 0 | 0 | Pericondensed |
| 154 | $C_{36}H_{16}$ | 6.0 | 2 | 8 | 6 | 0 | Irregular |
| 157 | $C_{42}H^-_{22}$ | 5.6 | 6 | 4 | 12 | 0 | Catacondensed, branched |
| 233 | $C_{23}H_{12}N^+$ | 5.4 | 0 | 12 | 0 | 0 | Pericondensed |
| 255 | $C_{52}H_{18}N^{+2}_2$ | 4.9 | 6 | 12 | 0 | 0 | Pericondensed |
| 704 | $C_{54}$ | 4.7 | 0 | 0 | 0 | 0 | 100% Dehydrogenated, pericondensed |
| 636 | $C_{48}H^+_{18}$ | 4.0 | 6 | 12 | 0 | 0 | Pericondensed |
| 31 | $C_{24}H^{+2}_{12}$ | 3.7 | 0 | 12 | 0 | 0 | Pericondensed |
| 549 | $C_{24}H^+_{14}$ | 2.8 | 0 | 0 | 6 | 8 | Catacondensed, branched |
| 601 | $C_{66}H^-_{20}$ | 2.7 | 7 | 10 | 3 | 0 | 5–7 Ring defects |
| 226 | $C_{23}H_{12}N$ | 2.1 | 0 | 12 | 0 | 0 | Pericondensed |
| 307 | $C_{22}H_{14}$ | 1.9 | 6 | 0 | 0 | 8 | Catacondensed, not branched |
| 568 | $C_{98}H^+_{28}$ | 1.8 | 14 | 8 | 6 | 0 | Pericondensed |
| 306 | $C_{22}H^+_{14}$ | 1.6 | 2 | 4 | 6 | 0 | Catacondensed, not branched |
| 108 | $C_{96}H_{24}$ | 1.4 | 12 | 12 | 0 | 0 | Pericondensed |
| 128 | $C_{36}H_{16}$ | 1.1 | 2 | 8 | 6 | 0 | Irregular |
| 234 | $C_{53}H_{18}N^+$ | 1.0 | 6 | 12 | 0 | 0 | Pericondensed |
| 544 | $C_{32}H^+_{18}$ | 0.9 | 4 | 0 | 6 | 8 | Catacondensed, branched |
| 639 | $C_{90}H^+_{24}$ | 0.8 | 12 | 12 | 0 | 0 | Pericondensed |
| 167 | $C_{112}H^-_{26}$ | 0.7 | 14 | 12 | 0 | 0 | Pericondensed |
| 627 | $C_{40}H^-_{16}$ | 0.7 | 4 | 12 | 0 | 0 | Pericondensed |
| 632 | $C_{128}H^+_{28}$ | <0.1 | 16 | 12 | 0 | 0 | Pericondensed |

Table 2.7: Results Derived From the Base Run on Features–Only Spectra

| | NGC 7023 NW | NGC 2023 | NGC 1333 |
|---|---|---|---|
| **Fit** | | | |
| Eucledian Norm* | 2.3 | 1.6 | 0.3 |
| Number of PAHs Used | 25 | 25 | 27 |
| **Size**** | | | |
| $x_{Nc<50}/x_{Nc>50}$ | 2.35 | 2.18 | 2.19 |
| **Ionization State**** | | | |
| $x_{PAH+}/x_{PAH0}$ | 0.79 | 0.94 | 0.79 |
| $x_{PAH+/++}/x_{PAH0}$ | 0.98 | 1.20 | 0.97 |
| $x_{PAH-}/x_{PAH0}$ | 0.32 | 0.41 | 0.27 |
| **Composition**** | | | |
| $x_{PANH}/x_{PAH}$ | 0.36 | 0.35 | 0.44 |
| **Structure** | | | |
| $n_{\rm duo}/n_{\rm solo}$ | 2.79 | 2.52 | 3.00 |
| $n_{\rm trio}/n_{\rm duo}$ | 0.15 | 0.17 | 0.13 |
| $n_{\rm quartet}/n_{\rm solo}$ | 0.16 | 0.19 | 0.12 |
| **Shape (%)** | | | |
| Compact Pericondensed (incl. 5–7) | 72.9 | 70.7 | 79.0 |
| Pericondensed With Edges (incl. 5–7) | 2.7 | 3.9 | 10.5 |
| Not Branched Catacondensed | 3.4 | 4.4 | 2.3 |
| Branched Catacondensed | 9.2 | 11.4 | 4.1 |
| Total contribution from PAHs with Defects | 2.7 | 3.5 | 1.3 |
| **Total contribution Pericondensed** | 75.6 | 74.6 | 89.6 |
| **Total contribution Catacondensed** | 12.6 | 15.8 | 6.3 |
| **Total contribution Irregular** | 7.1 | 4.9 | 0.1 |
| **Total contribution Completely Dehydrogenated** | 4.7 | 4.8 | 4.0 |

* The Eucledian Norm is defined as the square root of the residual sum of squares between the observed spectrum and the corresponding fit. ** All ratios are expressed in terms of the abundances of each species $x$. PAHs with $N_c < 50$ carbon atoms are considered to be small, while PAHs with $N_c > 50$ carbon atoms are considered to be large PAHs. In terms of ionization states, $PAH^0$ refers to neutral species; $PAH^{+/++}$ refers to all positively ionized PAHs; $PAH^+$ refers to only singly positively ionized PAHs; and $PAH^-$ refers to anionic species (PAHdb only contains singly negatively ionized PAHs). In terms of composition, $x_{\rm PANH}/x_{\rm PAH}$ refers to the abundance ratio of nitrogenated species relative to pure (carbon and hydrogen) PAHs. Hydrogen adjacency ratios are given in terms of the number of solo ($n_{\rm solo}$), duo ($n_{\rm duo}$), trio ($n_{\rm trio}$) and quartet hydrogens ($n_{\rm quartet}$), i.e. number of adjacent hydrogens attached to the same aromatic ring.

now PAHs with 5–7 ring *SW defects* contribute in only ~3% to the total abundance. Recent studies have concluded that PAHs having *SW defects* may be important members of the family of interstellar PAHs (Ricca et al. 2011; Yu & Nyman 2012). In principle, these PAHs appear to be important in the growth of edged-graphene structures, based on high temperature combustion models. These models are expected to resemble the physical conditions under which PAHs are presumably formed in the external envelopes of AGB stars (Whitesides & Frenklach 2010; Ricca et al. 2011). In terms of their mid-IR spectra, PAHs with *SW defects* show more bands than their non-defected analogues and, most importantly, they show C-C stretching bands at systematically different wavelengths around 6.2 $\mu$m. This has been used as an argument in favor of the presence of PAHs with *SW defects* in space, as it could potentially explain the observed differences in this band position between the A-B-C classes established in Peeters et al. (2002).

Table 2.8: New PAHs Used to Fit NGC7023 Features+Plateaus spectrum Without Admitting PAHs With SW Defects

| Uid | Formula | Abundance (%) | $n_{solo}$ | $n_{duo}$ | $n_{trio}$ | $n_{quartet}$ | Structure |
|---|---|---|---|---|---|---|---|
| 306 | $C_{22}H_{14}^{+}$ | 5.7 | 2 | 4 | 0 | 8 | Catacondensed, not branched |
| 568 | $C_{98}H_{28}^{+}$ | 2.3 | 14 | 8 | 6 | 0 | Pericondensed, with edges |
| 550 | $C_{24}H_{14}^{-}$ | 2.1 | 0 | 0 | 6 | 8 | Catacondensed, branched |
| 115 | $C_{66}H_{20}$ | 1.7 | 8 | 12 | 0 | 0 | Pericondensed |
| 233 | $C_{23}H_{12}N^{+}$ | 1.4 | 0 | 12 | 0 | 0 | Pericondensed |
| 242 | $C_{31}H_{14}N^{+}$ | 1.4 | 2 | 12 | 0 | 0 | Pericondensed |
| 173 | $C_{90}H_{30}^{-}$ | 1.0 | 18 | 12 | 0 | 0 | Irregular |
| 642 | $C_{144}H_{30}^{+}$ | 1.0 | 18 | 12 | 0 | 0 | Pericondensed |
| 535 | $C_{32}H_{18}$ | 0.8 | 4 | 0 | 6 | 8 | Catacondensed, branched |
| 171 | $C_{90}H_{30}$ | 0.6 | 18 | 12 | 0 | 0 | Irregular |
| 313 | $C_{21}H_{13}N^{+}$ | 0.4 | 6 | 0 | 0 | 8 | Catacondensed, not branched |

Figure 2.16 shows the normalized spectrum of the *SW defect* PAH of circumovalene anion $C_{66}H_{20}^{-}$ after absorbing a 7 eV photon. This PAH appears to be the second most abundant PAH in all *base run* fits to *Features+Plateaus* spectra, and in this figure we can clearly see why. It has several bands in the 6–9 $\mu$m region, and as such, the fitting procedure uses it to fit the plateaus. Once plateaus are removed, the contribution from PAHs with *SW defects* become negligible compared to the input from the other classes. In fact when performing the *base run* fit to *Features+Plateaus* spectra but removing all PAHs with *SW defects* from the initial pool (590 < uid < 609), we obtain good quality fits, where the abundance input from Stone-Wales PAHs is replaced by increasing the fraction of small cationic species containing slightly more irregular structures (quartet and trio-hydrogens). Interestingly we realize that PAHs with *SW defects* (especially $C_{66}H_{20}^{-}$) are also used to account for the 6.2 $\mu$m band. For NGC7023 *Features+Plateaus* spectrum the new fit uses 33 PAHs, from which 11 PAHs are not *base-run* ones. These 11 new PAHs contribute in 18.5% abundance (see Table 2.8). Stone-Wales PAHs then are replaced by generally increasing the abundance of small cationic original *base-run* PAHs ($x_{Nc<50}/x_{Nc>50}$ = 5.06; $x_{PAH+/++}/x_{PAH0}$ = 0.80; $x_{PAH-}/x_{PAH0}$ = 0.20); but also by adding new nitrogenated species, increasing their contribution to 44% compared to the 19% input derived from the fit admitting PAHs with *SW defects*. This refers to the need to reproduce the 6.2 $\mu$m feature once Stone-Wales PAHs are removed from the fit. We can affirm then that given the current state of PAHdb, both PAHNs and 5–7 ring defected species are, by default, used to fit the 6.2 $\mu$m feature. Therefore both contributions should be taken cautiously until our knowledge on PAH formation/destruction processes can give us further clues on which species are indeed expected to be more abundant in the ISM.

# 2.B. Tests on Model Parameters

## 2.B.1. Band Profile

All results shown in this work have been obtained from considering that PAH bands can be described by Gaussian profiles. Here we test how the *base run* results vary when considering Lorentzian profiles instead. In this case we are also considering a constant FWHM of 15 wavenumbers for each band, in order to only test the effect of changing the band profiles.

Comparing the results of the fits derived from using Gaussian profiles against Lorentzian ones, we see that the quality of both fits is quite similar (Eucledian norm of 2.0) just as the level of the

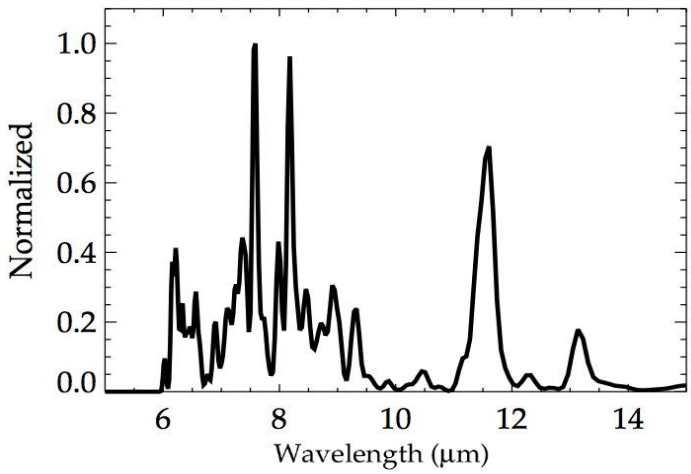


Figure 2.16: Emission spectrum of the SW *defect* PAH of $C_{66}H_{20}^{-}$ in the radiation field of NGC7023. The spectrum is shown in normalized scale. This PAH is the second most abundant PAH in all *base-run* fits of *Features+Plateaus* spectra. However when fitting *Features-Only* spectra, this PAH is not longer used in the fits. In fact the contribution of PAHs with 5–7 ring *SW defects* decreases to negligible levels for all three PDR spectra when compared to other species.

residuals (see Figure 2.17). The largest difference is in the number of different PAHs used in the fit, which in this case is lower (only 26 PAHs) than that of the *base run* using Gaussian profiles. This reflects the fact that Lorentzian profiles appear to fit better some PAH bands that otherwise have to be fitted with more than one Gaussian (Smith et al. 2007).

In terms of the PAHs themselves, out of the 26 PAHs used in this new fit, 21 of them correspond to original *base-run* PAHs. These 21 *base-run* PAHs contribute 95% to the total abundance of the PAHs in the new fit. Hence class ratios remain the same between both runs (ratios change in $<10\%$). The only ratio that does change is the $n_{quartet}/n_{solo}$ hydrogen adjacency ratio which decreases in $\sim 70\%$ its value from the one listed in Table 2.4 of the main text. This is because 3 out of the 5 PAHs with quartet hydrogens present in the *base-run* set are no longer used in this new fit. Interestingly all of these are catacondensed branched PAHs.

## 2.B.2. FWHM

Here we test what happens when we change the FWHM of the bands according to Bauschlicher et al. (2008). This approach considers a FWHM of 30 wavenumbers for bands at $\lambda < 9\,\mu$m; a FWHM of 10 wavenumbers for bands at $\lambda > 10\,\mu$m; and a FWHM that scales linearly from 30 to 10 wavenumbers in the 9–10 $\mu$m region.

The result of the fit is shown in Figure 2.18. The fit resembles that of the *base run*, which considers a constant FWHM for all bands. In terms of classes, there is a small increase in the cation/neutral fraction. The input from cations is now of 35% to the total abundance, against 26% in the original *base run*. Neutral species are still dominating the mixture then with an abundance contribution of 42% (against 48% in the *base run*).

In terms of the fit itself, we see the quality is similar. The new fit uses more PAHs: 44 compared to 33 in the original *base run*. Out of these 44 PAHs, 29 are *base-run* ones, and they contribute in $\sim 81\%$ to the total abundance of PAHs in the fit.

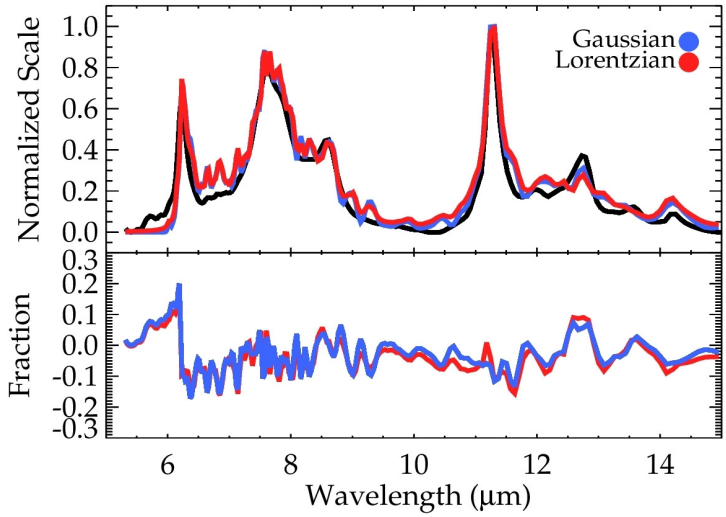


Figure 2.17: Base run fit to the *Features+Plateaus* spectrum of the brightest location in NGC7023 using Lorentzians to describe the profile of PAH bands (red curve). The *base run* fit using Gaussian profiles is also shown for a comparison (blue curve). The spectra are shown in normalized scale. The figure also shows the difference between both normalized spectra. For NGC7023 out of a pool of 292 PAHs, the fit ends up using 26 PAHs.

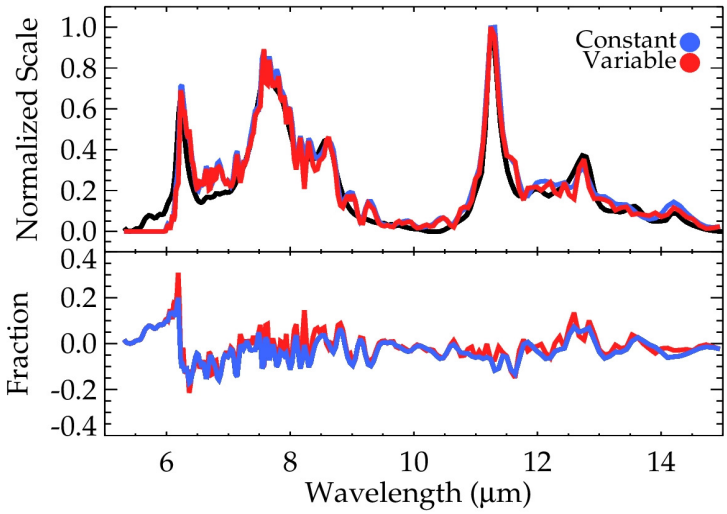


Figure 2.18: Base run fit to the *Features+Plateaus* spectrum of the brightest location in NGC7023 using variable FWHM depending on the wavelength range of the bands following Bauschlicher et al. (2008) (shown in red). The fit using a constant FWHM = 15 $cm^{-1}$ is shown in blue for a comparison. The figure also shows the difference between both normalized spectra. For NGC7023 out of a pool of 292 PAHs, the fit ends up using 44 PAHs, against the 33 used when considering a constant FWHM.

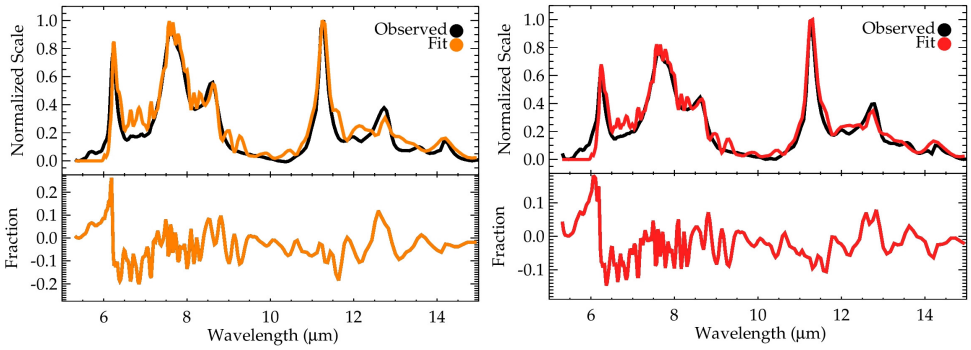


Figure 2.19: Base run fit to the *Features+Plateaus* spectrum of the brightest location in NGC 2023 (left) and NGC 1333 (right). The spectra are shown in normalized scale. The figure also shows the difference between both normalized spectra. For NGC 2023 out of a pool of 292 PAHs, the fit ends up using 31 PAHs (see Table 2.9). For NGC 1333, the fit ends up using 36 PAHs (see Table 2.10).

## 2.C. Base run fits to NGC 2023 and NGC 1333 spectra

Table 2.9: Base run PAHs derived from fit to NGC 2023 Features+Plateaus spectrum

| Uid | Formula | Abundance (%) | $n_{solo}$ | $n_{duo}$ | $n_{trio}$ | $n_{quartet}$ | Shape |
|---|---|---|---|---|---|---|---|
| 605 | $C_{66}H_{20}^{-}$ | 15.2 | 8 | 12 | 0 | 0 | 5–7 Ring defects |
| 128 | $C_{36}H_{16}$ | 13.0 | 2 | 8 | 6 | 0 | Irregular |
| 620 | $C_{42}H_{16}$ | 8.9 | 4 | 12 | 0 | 0 | Pericondensed |
| 226 | $C_{23}H_{12}N$ | 6.4 | 0 | 12 | 0 | 0 | Pericondensed |
| 157 | $C_{42}H_{22}^{-}$ | 5.1 | 6 | 4 | 12 | 0 | Catacondensed, branched |
| 636 | $C_{48}H_{18}^{+}$ | 5.0 | 6 | 12 | 0 | 0 | Pericondensed |
| 600 | $C_{66}H_{20}$ | 5.0 | 7 | 10 | 3 | 0 | 5–7 Ring defects, with edges |
| 255 | $C_{52}H_{18}N_{2}^{+2}$ | 4.9 | 6 | 12 | 0 | 0 | Pericondensed |
| 307 | $C_{22}H_{14}$ | 4.5 | 6 | 0 | 0 | 8 | Catacondensed, not branched |
| 11 | $C_{32}H_{14}^{-}$ | 4.2 | 2 | 12 | 0 | 0 | Pericondensed |
| 229 | $C_{23}H_{12}N$ | 3.6 | 0 | 12 | 0 | 0 | Pericondensed |
| 704 | $C_{54}$ | 3.2 | 0 | 0 | 0 | 0 | 100% Dehydrogenated, pericondensed |
| 592 | $C_{32}H_{14}^{+}$ | 3.0 | 2 | 12 | 0 | 0 | 5–7 Ring defects |
| 601 | $C_{66}H_{20}^{+}$ | 2.3 | 7 | 10 | 3 | 0 | 5–7 Ring defects, with egdes |
| 639 | $C_{90}H_{24}^{+}$ | 2.2 | 12 | 12 | 0 | 0 | Pericondensed |
| 31 | $C_{24}H_{12}^{+2}$ | 2.1 | 0 | 12 | 0 | 0 | Pericondensed |
| 158 | $C_{42}H_{22}^{+}$ | 2.1 | 6 | 4 | 12 | 0 | Catacondensed, branched |
| 544 | $C_{32}H_{18}^{+}$ | 2.0 | 4 | 0 | 6 | 8 | Catacondensed, branched |
| 243 | $C_{31}H_{14}N^{+}$ | 1.1 | 2 | 12 | 0 | 0 | Pericondensed |
| 632 | $C_{128}H_{28}^{+}$ | 0.9 | 16 | 12 | 0 | 0 | Pericondensed |
| 308 | $C_{22}H_{14}^{+}$ | 0.9 | 6 | 0 | 0 | 8 | Catacondensed, not branched |
| 614 | $C_{150}H_{30}^{-}$ | 0.7 | 18 | 12 | 0 | 0 | Pericondensed |
| 543 | $C_{36}H_{20}^{-}$ | 0.7 | 6 | 0 | 6 | 8 | Catacondensed, branched |
| 626 | $C_{40}H_{16}^{+}$ | 0.7 | 4 | 12 | 0 | 0 | Pericondensed |
| 37 | $C_{54}H_{18}$ | 0.5 | 0 | 12 | 0 | 0 | Pericondensed |
| 181 | $C_{102}H_{26}^{+}$ | 0.5 | 12 | 8 | 6 | 0 | Pericondensed, with edges |
| 114 | $C_{96}H_{24}^{-}$ | 0.3 | 12 | 12 | 0 | 0 | Pericondensed |
| 624 | $C_{170}H_{32}^{-}$ | 0.3 | 20 | 12 | 0 | 0 | Pericondensed |
| 108 | $C_{96}H_{24}$ | 0.2 | 12 | 12 | 0 | 0 | Pericondensed |
| 167 | $C_{112}H_{26}^{-}$ | 0.2 | 14 | 12 | 0 | 0 | Pericondensed |
| 171 | $C_{90}H_{30}$ | <0.1 | 18 | 12 | 0 | 0 | Irregular |

Table 2.10: Base run PAHs derived from fit to NGC 1333 Features+Plateaus spectrum

| Uid | Formula | Abundance (%) | $n_{solo}$ | $n_{duo}$ | $n_{trio}$ | $n_{quartet}$ | Shape |
|---|---|---|---|---|---|---|---|
| 128 | $C_{36}H_{16}$ | 15.2 | 2 | 8 | 6 | 0 | Irregular |
| 605 | $C_{66}H_{20}$ | 14.2 | 8 | 12 | 0 | 0 | 5–7 Ring defects |
| 620 | $C_{42}H_{16}$ | 8.8 | 4 | 12 | 0 | 0 | Pericondensed |
| 226 | $C_{23}H_{12}N$ | 6.7 | 0 | 12 | 0 | 0 | Pericondensed |
| 600 | $C_{66}H_{20}$ | 6.2 | 7 | 10 | 3 | 0 | 5–7 Ring defects, with edges |
| 11 | $C_{32}H_{14}^{-}$ | 4.4 | 2 | 12 | 0 | 0 | Pericondensed |
| 636 | $C_{48}H_{18}^{+}$ | 4.0 | 6 | 12 | 0 | 0 | Pericondensed |
| 157 | $C_{42}H_{22}^{-}$ | 3.8 | 6 | 4 | 12 | 0 | Catacondensed, branched |
| 255 | $C_{52}H_{18}N_{2}^{+2}$ | 3.5 | 6 | 12 | 0 | 0 | Pericondensed |
| 243 | $C_{31}H_{14}N^{+}$ | 3.2 | 2 | 12 | 0 | 0 | Pericondensed |
| 592 | $C_{32}H_{14}^{+}$ | 3.2 | 2 | 12 | 0 | 0 | 5–7 Ring defects |
| 591 | $C_{32}H_{14}$ | 2.8 | 2 | 12 | 0 | 0 | 5–7 Ring defects |
| 154 | $C_{36}H_{16}$ | 2.4 | 2 | 8 | 6 | 0 | Pericondensed, with edges |
| 284 | $C_{22}H_{12}$ | 2.4 | 0 | 6 | 6 | 0 | Irregular |
| 229 | $C_{23}H_{12}N$ | 2.1 | 0 | 12 | 0 | 0 | Pericondensed |
| 158 | $C_{42}H_{22}^{+}$ | 1.9 | 6 | 4 | 12 | 0 | Catacondensed, branched |
| 704 | $C_{54}$ | 1.9 | 0 | 0 | 0 | 0 | 100% Dehydrogenated, pericondensed |
| 639 | $C_{90}H_{24}^{+}$ | 1.7 | 12 | 12 | 0 | 0 | Pericondensed |
| 31 | $C_{24}H_{12}^{+2}$ | 1.2 | 0 | 12 | 0 | 0 | Pericondensed |
| 632 | $C_{128}H_{28}^{+}$ | 1.0 | 16 | 12 | 0 | 0 | Pericondensed |
| 543 | $C_{36}H_{20}^{-}$ | 1.0 | 6 | 0 | 6 | 8 | Catacondensed, branched |
| 29 | $C_{24}H_{12}^{-}$ | 1.0 | 0 | 12 | 0 | 0 | Pericondensed |
| 601 | $C_{66}H_{20}^{+}$ | 0.9 | 7 | 10 | 3 | 0 | 5–7 Ring defects, with edges |
| 305 | $C_{22}H_{14}$ | 0.8 | 2 | 4 | 0 | 8 | Catacondensed, not branched |
| 308 | $C_{22}H_{14}^{+}$ | 0.8 | 6 | 0 | 0 | 8 | Catacondensed, not branched |
| 181 | $C_{102}H_{26}^{+}$ | 0.7 | 12 | 8 | 6 | 0 | Pericondensed, with edges |
| 257 | $C_{52}H_{18}N_{2}^{+2}$ | 0.7 | 6 | 12 | 0 | 0 | Pericondensed |
| 624 | $C_{170}H_{32}^{-}$ | 0.7 | 20 | 12 | 0 | 0 | Pericondensed |
| 134 | $C_{42}H_{18}$ | 0.6 | 0 | 6 | 12 | 0 | Irregular |
| 626 | $C_{40}H_{16}^{+}$ | 0.6 | 4 | 12 | 0 | 0 | Pericondensed |
| 707 | $C_{66}^{+}$ | 0.5 | 0 | 0 | 0 | 0 | 100% Dehydrogenated, pericondensed |
| 167 | $C_{112}H_{26}^{-}$ | 0.5 | 14 | 12 | 0 | 0 | Pericondensed |
| 228 | $C_{23}H_{12}N^{+}$ | 0.3 | 0 | 12 | 0 | 0 | Pericondensed |
| 701 | $C_{96}H_{22}^{-}$ | 0.2 | 12 | 10 | 0 | 0 | Pericondensed, partially dehydrogenated |
| 544 | $C_{32}H_{18}^{+}$ | 0.1 | 4 | 0 | 6 | 8 | Catacondensed, branched |
| 614 | $C_{150}H_{30}^{-}$ | <0.1 | 18 | 12 | 0 | 0 | Pericondensed |

## 2.D. PAHs used in the base run fit to NGC7023

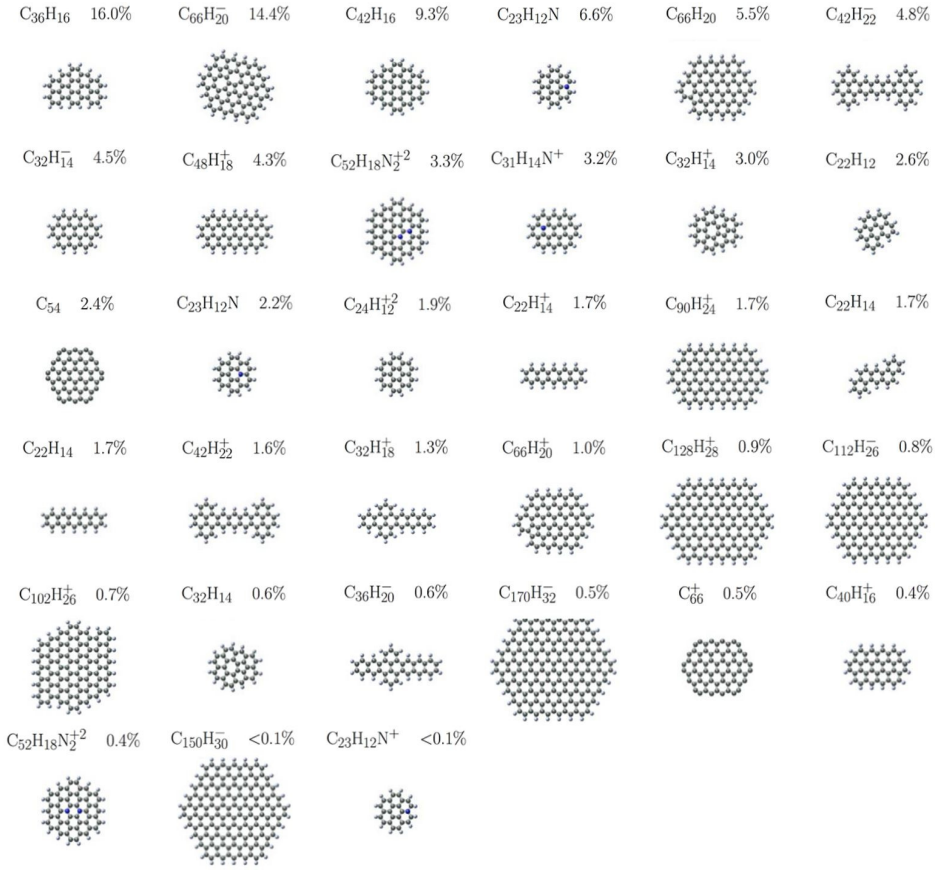


Figure 2.20: Base-run PAHs used in the fit to the *Features+Plateaus* spectrum of the brightest location in NGC7023. The formulae and relative abundances of each PAH are shown in the figure.